Feasibility of mechanical post-tensioning of annealed glass beams by activating externally bonded Fe-SMA reinforcement

Jorge Rocha , Eduardo Pereira [*], José Sena-Cruz

ISISE, IB-S, University of Minho, School of Engineering, Campus de Azurém, 4800-058 Guimarães, Portugal

ABSTRACT

The structural concept of post-tensioned glass systems has been investigated to minimize the unpredictable response of structural glass in tension. The Fe-SMAs have been successfully explored for strengthening existing structures due to their advantages in comparison with the conventional reinforcement materials. In particular, the recently developed Fe-17Mn-5Si-10Cr-4Ni-1VC (mass-%) alloy seems sustainable and shows promising properties for the construction industry. This study investigates the feasibility of post-tensioning glass beams by activating externally bonded Fe-SMA strips. The investigation is mainly focussed on (i) the activation process of Fe-SMA strips, with temperatures ranging between 120 °C and 160 °C, and (ii) the advantages of this reinforcement for post-tensioning of glass structural elements, in terms of applicability and structural response. Flexural tests show that it is possible to obtain ductile failure modes when glass beams are reinforced with passive or activated Fe-SMA strips. Activation of Fe-SMA strips resulted in an increase of up to 30 % of the cracking load.

1. Introduction

Although the theoretical tensile strength of glass is exceptionally high at the molecular scale, its effective tensile strength is much lower due to mechanical flaws resulting from the production, cutting, polishing and handling operations [1,2]. The tensile strength of glass is influenced by (i) surface conditions, i.e., the number and depth of initial flaws, (ii) size of the glass elements, (iii) loading history, i.e., intensity and duration, and (iv) residual stresses and environmental conditions [3]. The glass industry has developed improved processing methods, namely the tempering and the lamination [4,5]. A favourable stress field is created by the tempering, which restrains the propagation of existing surface flaws and increases the apparent tensile strength of glass. Glass lamination, on the other hand, uses a transparent polymeric interlayer to join glass plies in a single panel – following the concept of redundancy – to ensure the integrity of the structural element after cracking. Nevertheless, glass remains an extremely fragile material.

1.1. Glass composite systems

Several safety concepts have been developed based on the composite action between glass and reinforcement materials, such as timber (e.g.

[6,7]), steel (e.g. [8–11]), Carbon Fibre Reinforced Polymers, CFRP (e.g. [12–14]) and Glass Fibre Reinforced Polymers, GFRP (e.g. [5,15–19]) have been investigated. Due to the transfer of tensile stresses from the glass to the reinforcement through shear stresses in the adhesive joint, these composite glass systems show the ability to carry load even after glass cracking.

The tensile strength of annealed glass is unpredictable because surface flaws grow when exposed to long-term loads under environmental conditions. The higher the tensile stress, longer the loading duration and deeper the surface flaws, the lower the tensile strength of annealed glass [3]. Tempering has been successful at preventing this unpredictability. However, tempered glass failure is catastrophic and results in small shards, compromising its structural integrity and, consequently, the post-failure residual strength/reserve and ductility of composite systems [4,5,18]. Heat-strengthened glass provides an interesting compromise between fairly high tensile strength and sufficiently large fragmentation patterns. In any case, annealed glass has obvious economic and structural benefits for the construction industry [20].

In order to overcome the unpredictability of the tensile strength of glass and make it safer for structural applications, the structural concept of post-tensioned glass systems has been recently investigated, using steel (e.g. [9,11,21]), CFRP (e.g. [12]) and SMA (e.g. [48]) as

reinforcement. These studies, yet reduced in number, have addressed different strategies concerning (i) the relative position of the reinforcement element; (ii) the post-tensioning setup; and (iii) the anchorage strategy to transfer the post-tensioning force from the reinforcement to the glass. While Bos et al. [9] and Louter et al. [11] positioned the reinforcement within the glass panel, Jordão et al. [21] and Louter et al. [12] placed it externally. In relation to the post-tensioning setup, the reinforcement has been positioned as a straight line along the glass panel (e.g. [12]) or adopting a layout resembling the bending moment curve shape (e.g. [21]). Concerning the anchorage strategy, the reinforcement has been mechanically anchored (e.g. [11]) and/or adhesively bonded to the glass (e.g. [12]).

Although the post-tensioned glass systems were proved to be effective, the procedure for applying post-tensioning is sometimes challenging because (i) heavy equipment is required, e.g. hydraulic actuators; and (ii) high stress concentrations are induced in the glass substrate when the prestressed reinforcement is released. As the tensile strength of annealed glass depends on the surface conditions and loading history [3], appropriate safety measures must be taken to ensure that the post-tensioning force is smoothly transferred from the reinforcement to the glass, preventing the premature failure of the glass due to the growth of existing surface flaws [22].

1.2. SMAs in civil engineering

Shape Memory Alloys (SMAs) have been used in civil engineering applications (e.g. buildings and bridges), reducing the effort and time involved in post-tensioning actions in comparison to conventional reinforcement materials (e.g. steel and CFRP). SMAs have shown to be advantageous due to two main characteristics: (i) the *shape memory effect*, which is the capability of the deformed material to partially return to its initial shape when heated above the activation temperature; and (ii) the *superelasticity*, which refers to the property according to which the material undergoes large and not necessarily linear mechanical deformations, but can still recover its initial shape after unloading and without the need for any thermal activation [23,24].

SMAs have been used for different fields of the civil engineering. While superelasticity is used to increase the damping and energy dissipation of reinforced concrete structures during earthquakes (e.g. [25,26]), the shape memory effect is appropriate for the post-tensioned strengthening of structural elements (e.g. [27–32]). When the SMA reinforcement is properly anchored (e.g. adhesively bonded and/or mechanically anchored) to the structural element prior to its activation, recovery stresses (post-tensioning forces) are developed by heating and subsequent cooling of the SMA material. The simplicity of this post-tensioning technique has enhanced the applicability of SMAs for the post-tensioned strengthening of existing structures, where the conventional procedure with hydraulic jacks is often difficult to implement due to lack of space [24,33].

The most recognized SMA is the nickel-titanium (Ni-Ti) alloy, which has been used in the automotive, aerospace, robotic, biomedical and construction industries for both sensory and structural (e.g. damper and reinforcement) purposes [23]. However, the Ni-Ti alloy may hardly be considered as a sustainable solution for generalized applications in the construction industry [30]. In construction, the material usage is several orders of magnitude larger when compared to other industries and, therefore, low-cost and less resource-intensive SMAs have been applied in this case, namely the iron-based (Fe-SMAs) and the copper-based (Cu-SMAs) alloys. Fe-SMAs are relatively low cost and easy to process, machine and weld, thus making them the most promising candidates for the application in the construction industry, whether for repairing existing structures or for reinforcing new ones [24,34].

In 1982, Sato et al. [35] discovered shape memory effect in Fe-Mn-Si alloys. Since then, the chemical composition of Fe-SMAs has been improved to increase their corrosion resistance, training effect, cyclic deformation and strength [36]. In this context, a new Fe-SMA, suitable

for the construction industry, was developed in 2009 by Dong et al. [37] at the Swiss Federal Laboratories for Materials Science and Technology (Empa), Switzerland. This Fe-SMA, which can be activated by resistive heating, was especially developed for the post-tensioned strengthening of existing concrete structures. In addition, it is produced at atmospheric conditions, without the need for expensive high-vacuum processing facilities and thermomechanical training, making the large-scale production feasible [30,38]. Research studies have shown the potential of the newly developed Fe-SMA for the post-tensioned strengthening of concrete, using strips (e.g. [29,30,39,40]) or ribbed bars (e.g. [41,42]), and metallic (e.g. [27,28,33]) structural elements. Further research studies have been conducted to show the potential of this Fe-SMA for structural engineering applications, investigating aspects related to the fatigue behaviour (e.g. [38]), phase transformation (e.g. [40]), creep and stress relaxation (e.g. [43]), electrochemical and corrosion behaviour (e.g. [44]) and recovery stress (e.g. [45]).

The application of SMAs as reinforcement material in glass composite systems is a very recent research field and, consequently, very few studies are found in the literature addressing this topic. They have focused on the bond behaviour of glass-to-SMA adhesively bonded joints (e.g. [46,47]). In addition, Silvestru el at. [48] proved, for the first time, the feasibility of activating Fe-SMA reinforcement to introduce an initial compressive pre-stress in laminated glass beams. Furthermore, the results showed that SMA reinforced glass elements can exhibit ductile failure modes.

1.3. Research significance

This study investigates the feasibility of the post-tensioning of monolithic glass beams by activating Fe-SMA strips previously bonded to the bottom edge, according to the External Bonded Reinforcement (EBR) technique, as well as the influence of the activation temperature on their post-cracking performance. After being bonded with an epoxy adhesive to the glass substrate, Fe-SMA strips were heated at temperatures ranging between 120 °C and 160 °C to activate them and introduce post-tensioning in the glass elements. The experimental programme comprised (i) mechanical characterization tests and (ii) full-scale bending tests. This study also addresses the opportunity to adapt the Fe-SMA reinforcement activation procedure in order to take advantage of initially deleterious effects, such as the degradation of the adhesive due to temperature exposure, in favour of an optimized anchorage and the gradual stress transfer from the reinforcement to the glass substrate.

2. Experimental programme

Two different types of experimental tests were carried out in the scope of this work: (i) first, material characterization tests were conducted to determine the mechanical properties of the Fe-SMA material and (ii) second, four-point bending tests were carried out to assess the flexural behaviour of annealed glass beams strengthened with passive Fe-SMA strips (reference beams) and activated Fe-SMA strips (post-tensioned beams).

2.1. Materials

2.1.1. Iron-based shape memory alloy (Fe-SMA)

In this research, the Fe-17Mn-5Si-10Cr-4Ni-1(V,C) (mass%) alloy with shape memory effect, developed by Dong et al. [37], was used as a reinforcement material for glass beams. Its detailed production procedure is described by Leinenbach et al. [49]. The industrial production of this Fe-SMA is ensured by re-fer AG Company, which offers two distinct products: (i) ribbed bars; and (ii) plates with thicknesses of 0.5 and 1.5 mm and widths of 50 and 100 mm. In this study, Fe-SMA plates of 100 (width) × 1.5 (thickness) [mm] were used to extract strips of 1500 (length) × 10 (width) × 1.5 (thickness) [mm]. The Fe-SMA strips were cut using the water jet technique to avoid overheating the Fe-SMA

material. Specimens were also extracted to characterize the Fe-SMA's tensile behaviour.

Five specimens of 250 (length) × 10 (width) [mm] were tested in tension at ambient temperature and at a constant displacement rate of 1.0 mm/min until failure. Prior to testing, 50 mm long tabs were glued to the edges of the Fe-SMA strips to avoid premature failure of the specimen due to stress concentrations introduced by the clamping equipment. The longitudinal deformation of each specimen was measured using a clip gauge (type: MFA 12; linearity: 0.1 %; sensitivity: 2.0 mV/V; resolution: 1.0p.m.; precision: ±1.5 μm) with stroke of 50 mm, which was placed at the central region of the specimens (see Fig. 1a). A universal testing machine and a load cell with a maximum capacity of 200 kN (precision of 0.01 kN) were used to record the load. Furthermore, some specimens were monitored with the Digital Image Correlation (DIC) technique and using the GOM Correlate 2019 software [50] for processing the images. A thin spray of white matt paint was applied over a region of interest, followed by a spray of black dots using black paint. The camera used to capture the images included a full frame CMOS sensor (7360 × 4912 pixels). The images of the ROI were collected at an acquisition frequency of 0.1 Hz.

Table 1 includes the average values obtained for the modulus of elasticity (E_r), tensile strength ($f_{r,t}$) and ultimate strain ($\varepsilon_{r,ult}$). As the Fe-SMA shows a highly non-linear behaviour, E_r was determined from the linear portion of the stress–strain response between stress values of 0 MPa and 200 MPa. The mechanical properties indicated in Table 1 compare well with the values found in the literature for this Fe-SMA. The modulus of elasticity of 172 GPa lies in the range of previously published values, between 160 GPa [45] and 175 GPa [38]. With respect to the tensile strength, 948.1 MPa is also an intermediate value between 939.3 MPa by Silvestru *et al.* [47] and 1015 MPa by Ghafoori *et al.* [38]. However, the ultimate strain of 31.0 % is lower than the values reported in the literature, usually higher than 40 %. The main reason for this difference seems to be displacement rate between clamps, which in this study was set to 1.0 mm/s while literature values ranging between 0.012 mm/s [47] and 0.075 mm/s [38] are mentioned.

Fig. 1b shows the typical stress – strain experimental response obtained from both measurement methods. Given the good agreement between the DIC and clip gauge measurements, the Poisson's ratio was

Table 1
Mechanical properties of the Fe-SMA material, annealed glass and 3 M adhesive (average values).

Material	E_r [GPa]	$f_{r,t}$ [MPa]	$\varepsilon_{r,ult}$ [%]	v [-]
Fe-SMA	172.0 (1.7 %)	948.1 (0.6 %)	32.5 (2.3 %)	0.39
Material	E_g [GPa]	$f_{g,t}$ [MPa]	$\varepsilon_{g,ult}$ [‰]	v [-]
Annealed glass a)	74.0 (2.6 %)	40	–	0.23
Material	E_{adh} [MPa]	f_{adh} [MPa]	$\varepsilon_{adh,ult}$ [‰]	v [-]
Adhesive a)	1728.1 (3.3 %)	32.8 (4.2 %)	30.7 (2.8 %)	0.38

Notes: Coefficients of variation (CoV) are indicated in parenthesis. a) Results collected from Rocha *et al.* [51].

determined from the deformation fields at the surface of the specimens and assuming plane stress state. Fig. 1b shows the obtained Poisson's ratio as a function of the axial strain. Unexpectedly, at the beginning of loading, the Poisson's ratio reached values of approximately 2.0, which gradually decreased to 0.39 at the end of the stress – strain response. Such response seems to be related to the phase change behaviour of the SMA materials. During the martensitic transformation, at the beginning of the stress – strain response, axial deformation is associated to the lattice detwinning. On the other hand, after martensitic transformation, at the end of the stress – strain response, further axial deformation is associated to the permanent and irreversible slip between atomic planes (yielding). Hence, at this final stage, the Fe-SMA Poisson's ratio converges to values exhibited by traditional materials (e.g. steel).

2.1.2. Glass and adhesive

All specimens used in the experimental programme were made of annealed glass. Laminated glass was not considered at this stage of the research because the interlayer may be significantly damaged during the heating of Fe-SMA strips, leading to layering of the glass plies. This effect, which is difficult to measure experimentally, may introduce uncertainty in the structural response of post-tensioned beams. The edges of the annealed glass panels were polished to minimize the flaws resulting from the cutting process and to prevent accidents during handling. The mechanical properties of the annealed glass shown in Table 1 were previously assessed by Rocha *et al.* [51], with the tensile
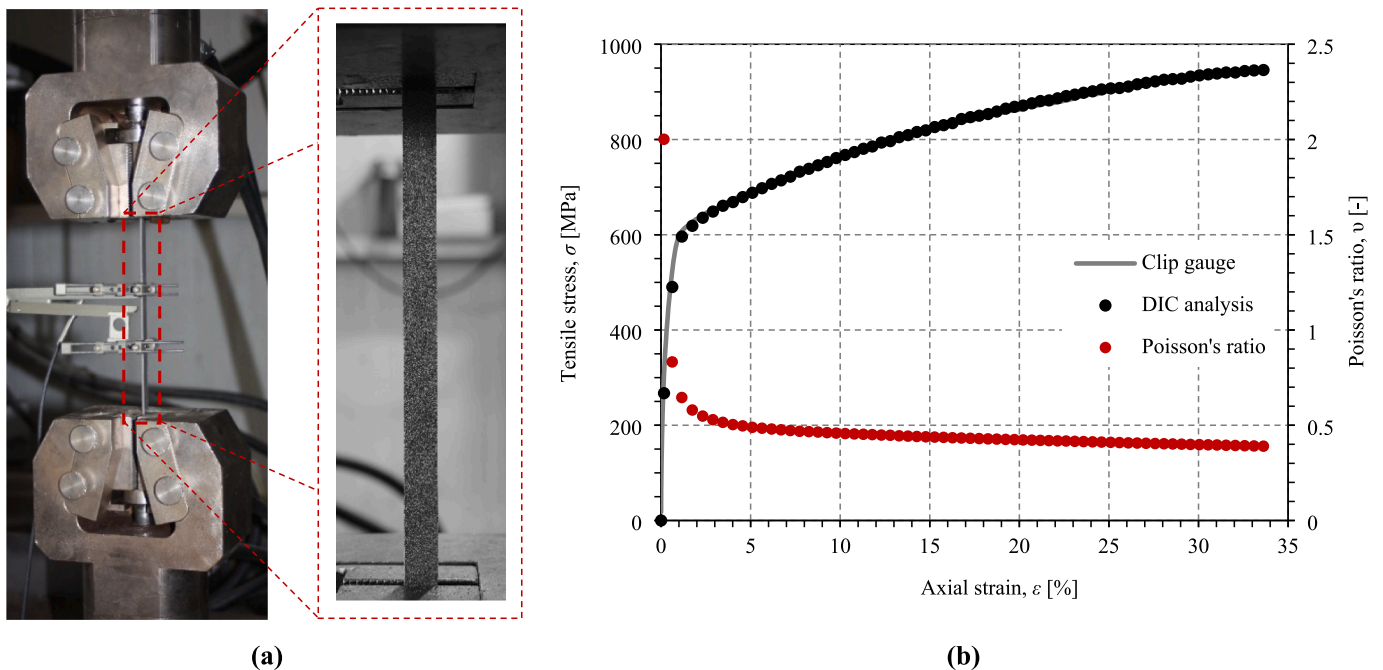

Fig. 1. Tensile tests on Fe-SMA strips: (a) experimental setup; and (b) stress–strain response obtained from both measurements methods, as well as evolution of the Poisson's ratio.

strength ($f_{g,t}$) and the modulus of elasticity (E_g) equal to 40 MPa and 74.0 GPa, respectively.

An epoxy adhesive, the two-component adhesive 3 M Scotch-Weld DP490, suitable for glass-to-steel bonded connections was used in these experiments. The tensile behaviour of this adhesive was previously characterized by Rocha et al. [51]. Its mechanical properties are presented in Table 1, including the Poisson's ratio determined by Nhamoinesu and Overend [52]. The adhesive presents a non-linear behaviour in tension until failure, combining a high tensile strength (f_{adh}) of 32.8 MPa with a relatively low modulus of elasticity (E_{adh}) of 1728.1 MPa, as well as an ultimate strain ($\varepsilon_{adh,ult}$) of 30.7 ‰.

2.2. Production and testing of the specimens

As schematically shown in Fig. 2, the application of Fe-SMA strips for post-tensioning of structural elements consists of three main phases: (i) pre-straining; (ii) activation; and (iii) service loading. The post-tensioning procedure will be briefly explained in this section. First, the Fe-SMA strip is mechanically loaded (path (1) in Fig. 2) at room temperature, between M_s (martensite start temperature) and A_s (austenite start temperature), modifying the lattice from austenite to detwinned martensite (i.e., martensitic transformation). When the target strain is attained, the Fe-SMA is then completely unloaded (path (2) in Fig. 2), then presenting a permanent macroscopic deformation. Second, the Fe-SMA strip is mechanically anchored and/or adhesively bonded to the structural element. Third, the Fe-SMA strip is activated through resistive heating (path (3) in Fig. 2) and, when A_s is surpassed, the restrained Fe-SMA strip tends to shrink due to the reverse transformation from detwinned martensite to austenite. Consequently, tensile stresses (i.e., recovery stresses) are developed in the Fe-SMA strip, recovering the thermal expansion observed at the beginning of the thermal cycle. When the target temperature is attained, heating of the Fe-SMA strip is stopped and the recovery stress gradually increases during the cooling phase, until the ambient temperature is reached again (path (4) in Fig. 2). Further details related to the behaviour of Fe-SMA during the activation can be found in the literature (e.g. [38,53]).

Taking into account the procedure mentioned above, the post-tensioned glass beams were prepared considering the following steps:

(i) cutting the Fe-SMA strips; (ii) pre-straining the Fe-SMA strips; (iii) bonding the Fe-SMA strips to the bottom edge of the glass panels; and (iv) activating the Fe-SMA strips using a resistive heating device. The reference beams were manufactured considering only the first and third steps. On the other hand, the bonding of Fe-SMA strips – the third step of the general procedure – involved additional paths. First, the bonding surfaces were carefully degreased and cleaned with acetone. Subsequently, the adhesive was prepared and applied according to the requirements included in the manufacturer specifications. After that, both adherends were assembled and then slightly pressed against each other in order to reach a pre-defined adhesive layer thickness. Finally, all specimens were placed in a climatic chamber at 30 °C during 7 days.

The glass-SMA composite beams were manufactured considering the geometry shown in Fig. 3, which consisted of an annealed glass panel of 100 (height) × 12 (thickness) [mm] reinforced at the bottom edge with a Fe-SMA strip of 10 (width) × 1.5 (thickness) [mm]. The components were joined using the epoxy adhesive presented in Section 2.1. The thickness of the adhesive joint (t_a in Fig. 3) was set to 0.3 mm. A total of 6 glass-SMA composite beams were produced, namely two reference beams with passive Fe-SMA strips and four post-tensioned beams with activated Fe-SMA strips. They were identified following the nomenclature *i-j-z*, where *i* distinguishes reference beams (R) from post-tensioned beams (P), *j* refers to the activation temperature (T0 for reference beams and T120, T140 and T160 for post-tensioned beams – further details in Section 2.2.2) and *z* identifies the specimens of each series with the same activation temperature (I and II).

2.2.1. Pre-straining of Fe-SMA strips

The amount of recovery stress depends on the amount of martensite in the Fe-SMA. Investigations conducted by Shahverdi *et al.* [30] on the Fe-SMA used in this study showed that a pre-strain (ε_{pre}) of 2.0 % is sufficient to achieve the maximum possible recovery stress. Therefore, before bonding the Fe-SMA strips to the glass substrate, these were pre-strained up to 2.25 % at room temperature. After unloading, the Fe-SMA strips showed a permanent remaining deformation (ε_{rem}) of approximately 1.25 %. Only a portion of the ε_{rem} could be recovered by activation (recovery strain) since the non-linear behaviour exhibited during pre-straining was a consequence of the phase transformation from
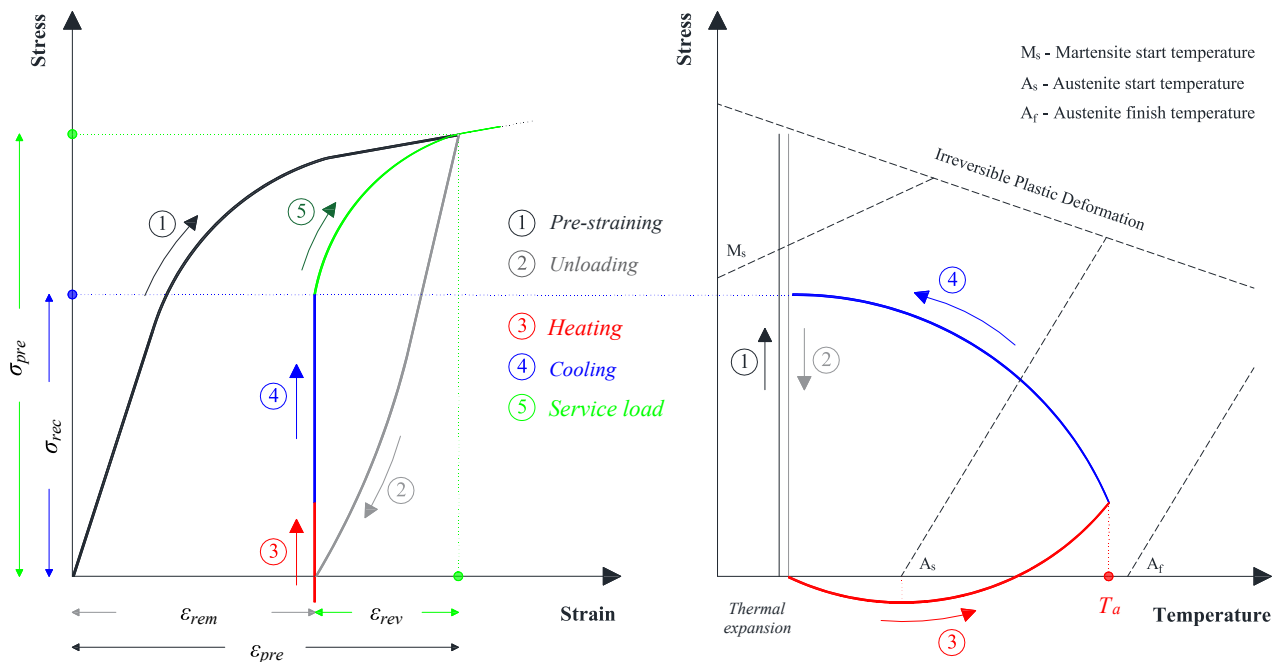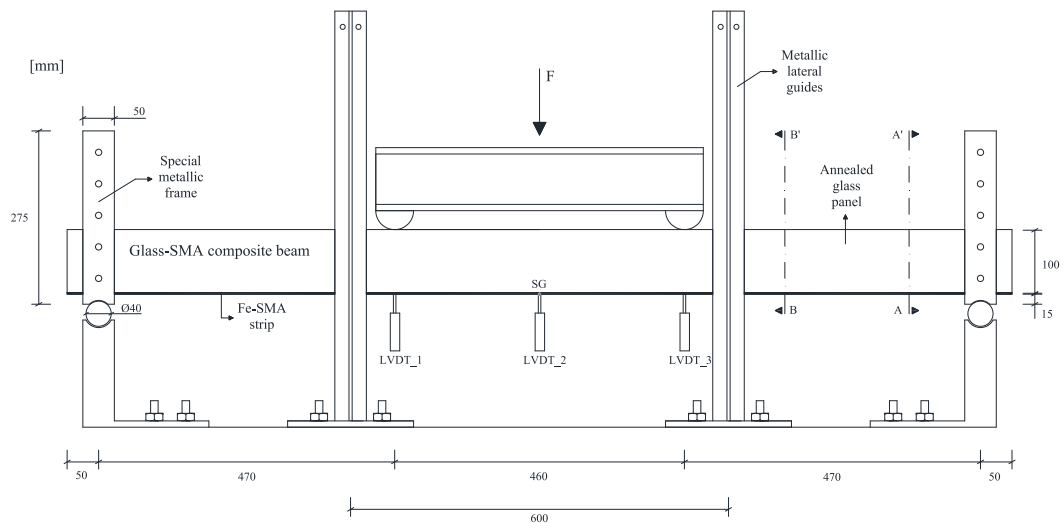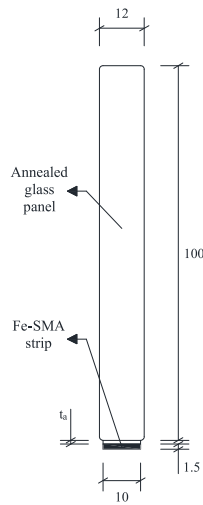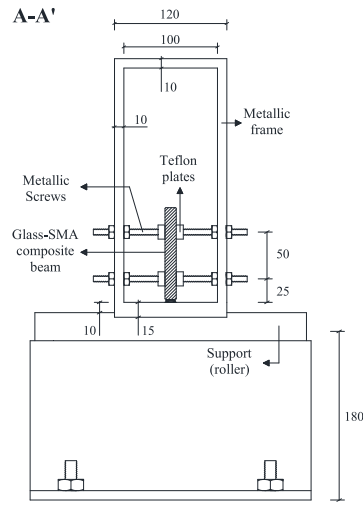

Fig. 2. Schematic representation of the activation procedure of Fe-SMAs under strain recovery constraint (red colour) adapted from Shahverdi *et al.* [29]. (For interpretation of the references to colour in this figure legend, the reader is referred to the web version of this article.)
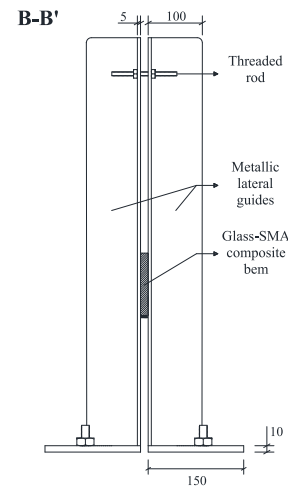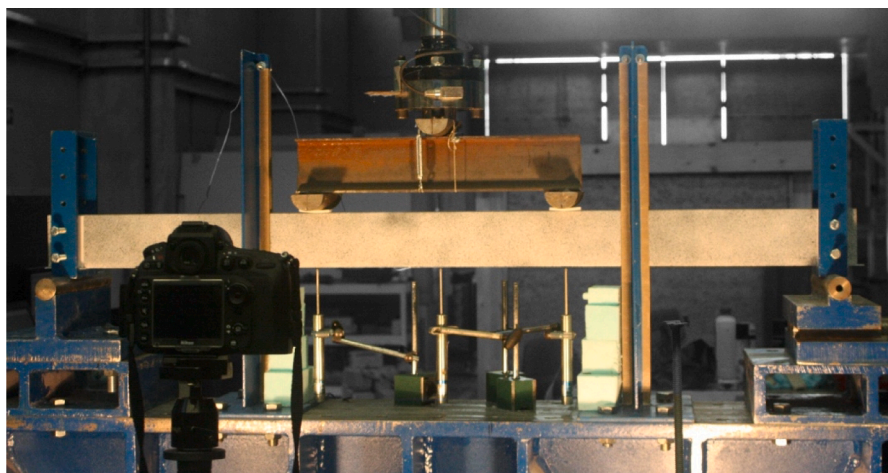
(a)

(b)   **(c)**   **(d)**

(e)

Fig. 3. Pre-straining of Fe-SMAs: (a) schematic diagram (b) stress–strain diagram retrieved from the experiments.

austenite to martensite, as well as the plastic deformation (irreversible slippage between atoms) [45]. As shown in Fig. 4, the deviation from the linear elastic unloading is called pseudo-elastic strain, indicating that the reverse transformation from martensite to austenite occurred partially during unloading [45]. The longitudinal deformation in the Fe-SMA strips was measured using a clip gauge (the same used for the characterization of the Fe-SMA described in Section 2.1.1) with a gauge length of 100 mm. A universal testing machine was used to apply the load.

2.2.2. Activation procedure

Glass contains numerous surface flaws that result from the production, cutting, polishing and handling processes [1]. In addition, glass edges typically have lower tensile strength than glass surfaces [54]. Accordingly, a smooth transfer of the post-tensioning force from the reinforcement to the glass panel must be guaranteed to avoid the growth of existing surface flaws over time, especially near the glass corners, which are usually weaker than the glass surfaces due to the handling operations. In addition, based on previous studies on the activation of adhesively bonded SMA reinforcement (e.g. [47,55]), an undamaged bond region (anchorage zone) should be guaranteed on both sides of the activated Fe-SMA strip zone to transfer the post-tensioning force from the reinforcement to the glass substrate. These anchorage zones prevent premature debonding of the Fe-SMA strip during activation due to the loss of shear interaction at the bonded interfaces caused by heating. Accordingly, the Fe-SMA strips should not be activated throughout its entire length.

As shown in Fig. 5a, the activated length (l_a) was set to 700 mm (half of the beam span), creating an undamaged bond length of 400 mm at both beam ends (non-activated Fe-SMA strip zones). A welding machine was used to supply the electrical power (see Fig. 5b). Two metallic pieces were symmetrically positioned at 350 mm from the mid-span section and subsequently pressed against the bottom edge of the Fe-SMA strip by means of metal clamps (see Fig. 5c and d). After that, the electrode holder and the ground clamp were connected to these metallic pieces, creating a circuit where the electrical current flowed from the former to the latter. Polytetrafluoroethylene (Teflon) plates were positioned between the metallic pieces and the metal clamps, for safety.

A relatively high current density of ∼ 4.0 A/mm² was adopted to shorten the heating phase as much as possible, in order to reduce the heat flow into the non-activated Fe-SMA strip zones. Different activation temperatures (T_a) were adopted to activate the Fe-SMA: (i) 120 °C for the P_T120 beams, (ii) 140 °C for the P_T140 beam, and (iii) 160 °C for

the P_T160 beam. The power supply was interrupted when the target temperature was attained. The activation process was assumed complete when the temperature on the Fe-SMA strip reached the room temperature again.

Fig. 5a shows the instrumentation adopted for the activation process. The deflection at the mid-span section of the Fe-SMA reinforced glass beams was measured using a displacement transducer – Linear Variable Differential Transformer (LVDT) – with stroke of 50 mm and precision of 0.01 mm. Furthermore, a strain gauge (type: BFLA-5–3-3L by TML; gauge length: 5 mm; gauge factor: 2.08 ± 1 %) was placed at the top edge of the glass panel. On the other hand, an infrared camera (Type: FLIR T420; temperature range: −20 to 650 °C; spectral range: 7.5 to 13 μm) was used to monitor the temperature evolution in the Fe-SMA strip during the activation process. User-defined parameters required by the infrared camera (e.g. emissivity) were previously calibrated using a type K thermocouple (see Fig. 6). For the sake of simplicity, only a small part of the Fe-SMA strips (≈ 20 mm in length) was monitored by the infrared camera (control region), therefore assuming a constant temperature along the activated length. The infrared camera was positioned so that only the Fe-SMA strip was captured by the control region (see Fig. 7), in order to avoid de influence of the emissivity of other components on the maximum temperature registered within the control region, which was taken as the effective activation temperature.

2.2.3. Bending tests

As shown in Fig. 3, the glass-SMA composite beams, with a span of 1.4 m, were tested adopting a symmetrical four-point bending configuration, with load points 460 mm apart. In order to avoid the direct metal-glass contact and the premature failure of composite beams, Teflon plates were positioned between the steel pieces and the glass. As shown in Fig. 3c, two pairs of vertical metallic guides were symmetrically positioned at 300 mm from the mid-span section to prevent lateral displacements (e.g. lateral-buckling effect). Each pair was joined by means of threaded rods to enhance the out-of-plane flexural stiffness. The surfaces of these lateral guides were carefully wrapped with a thin Teflon film to prevent frictional forces during tests, as well as direct metal-glass contact.

In-plane flexural rotations were free at both supports, and one of the supports allowed the longitudinal sliding of the beams. As illustrated by Fig. 3a, metallic frames specially designed were placed overhead the supports to restrain out-of-plane rotations at the support sections. After positioning the composite beams, the threaded screws of metallic boxes were carefully pressed against the glass, using intermediate Teflon plates
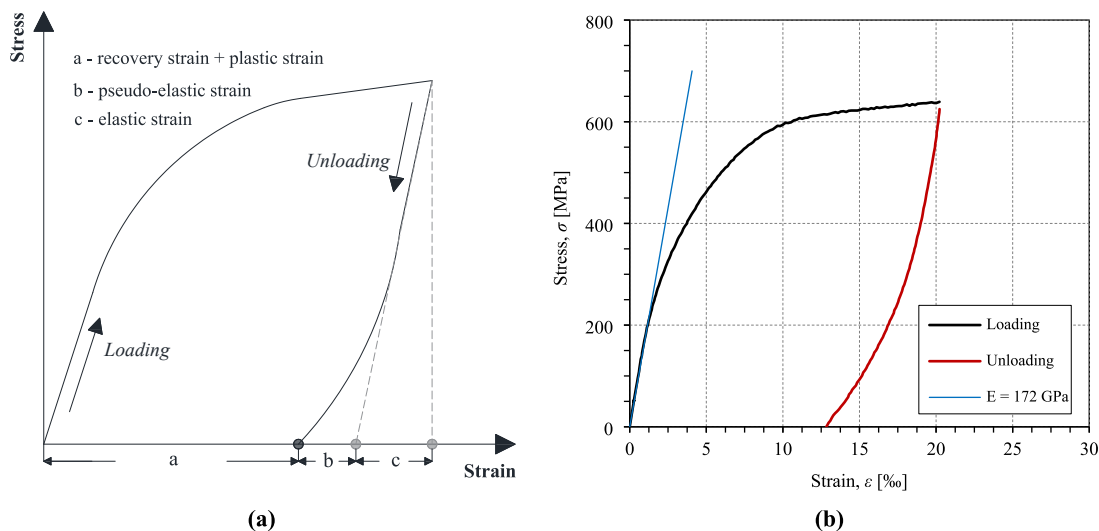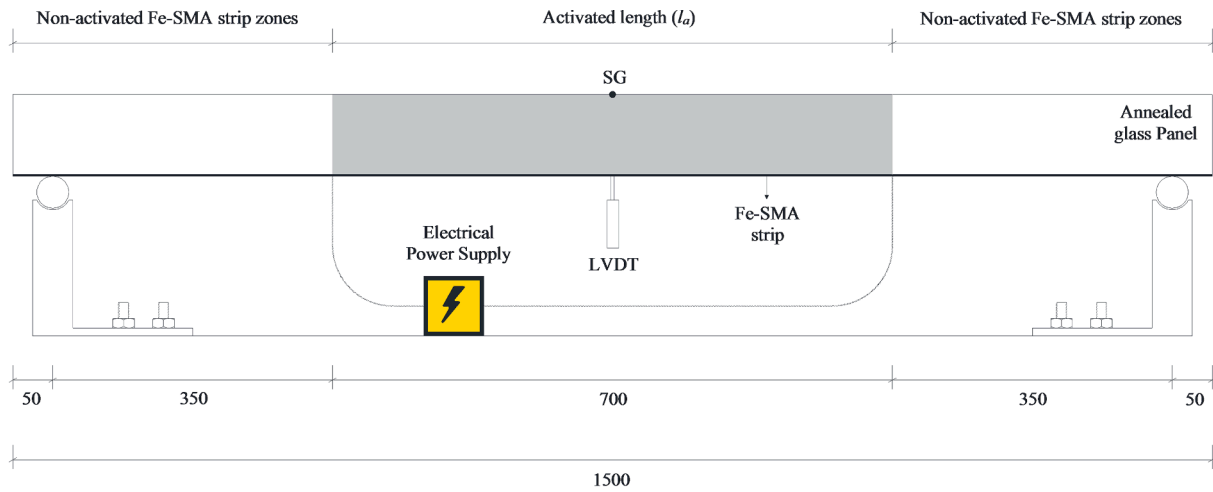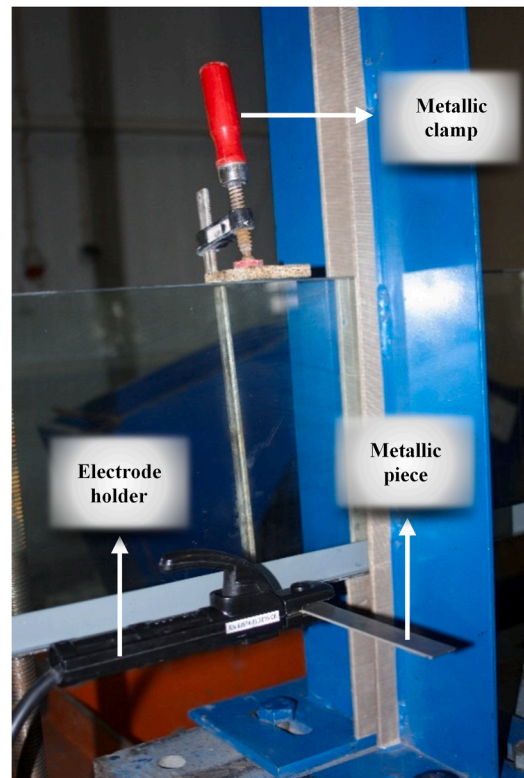

Fig. 4. Glass-SMA composite beams: (a) beam geometry and instrumentation adopted for the bending tests; (b) cross-section geometry; (c) metallic frames placed at the support sections; (d) lateral guides to prevent lateral instability; and (e) experimental setup. All units in [mm].
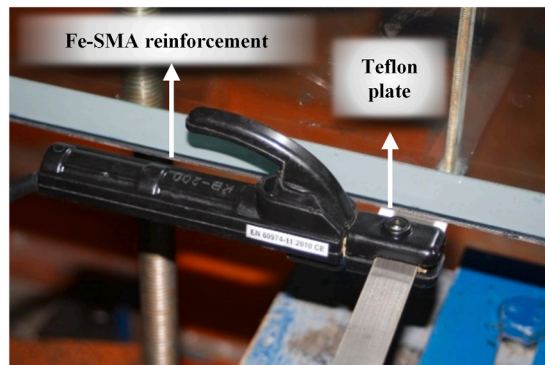
Fig. 5. Activation of the Fe-SMA strips: (a) activated region and adopted strategy; (b) welding machine used to supply electrical power for the activation process; and (c) and (d) connection between the welding machine clamps and the Fe-SMA reinforcement. All units in [mm].

to avoid glass-steel contact.

Fig. 3a shows the LVDTs used in these experiments: LVDT_1 and LVDT_3 measured the deflections at loading point sections, while the LVDT_2 measured the mid-span deflection. These LVDTs have equal characteristics to the ones referred in Section 2.2.2. Axial strains in the Fe-SMA strips were also measured at the mid-span section using a strain gauge (type: PFL-10–11-3LJC-F by TML; gauge length: 10 mm; gauge factor: 2.12 ± 1 %). A load cell with a maximum measuring capacity of 200 kN and a linearity error of $\pm$ 0.05 % was used to measure the applied load. All test specimens were loaded monotonically under displacement control at a speed of 1.0 mm/min (internal LVDT of the actuator). While, the applied load and the deflections were measured

using a relatively high acquisition frequency of 50 Hz to capture sudden phenomena resulting from the low fracture energy of the glass, axial strains were recorded at a frequency of 3 Hz due to limitations on the acquisition system. The tests were conducted in laboratory environment at an average temperature of 26 °C and relative humidity of 65 %.

The Digital Image Correlation (DIC) method was also used to document the evolution of cracking and the formation of resisting mechanisms in glass-SMAs composite beams. Further details about the DIC method can be found in Section 2.1.1, including the characteristics of the camera used.
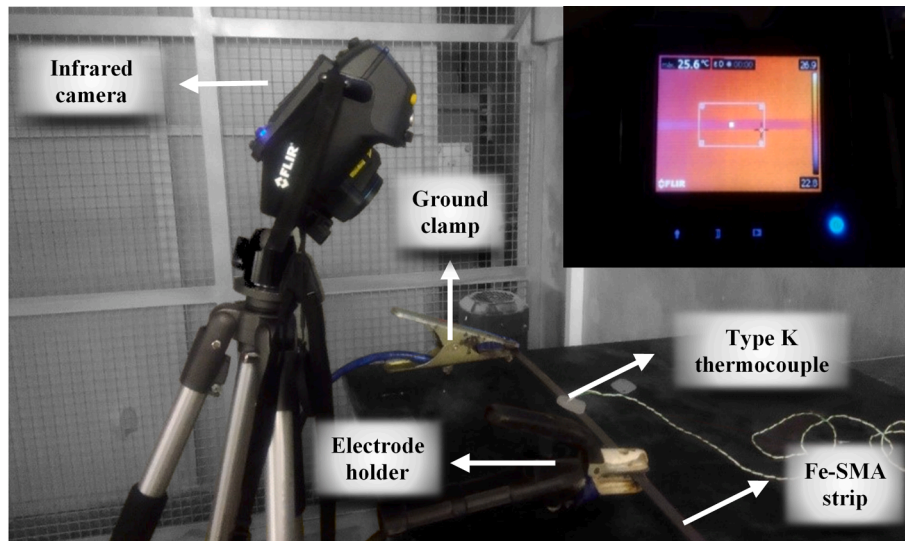
Fig. 6. Preliminary experiments conducted to determine the user-defined variables required by the thermographic camera.
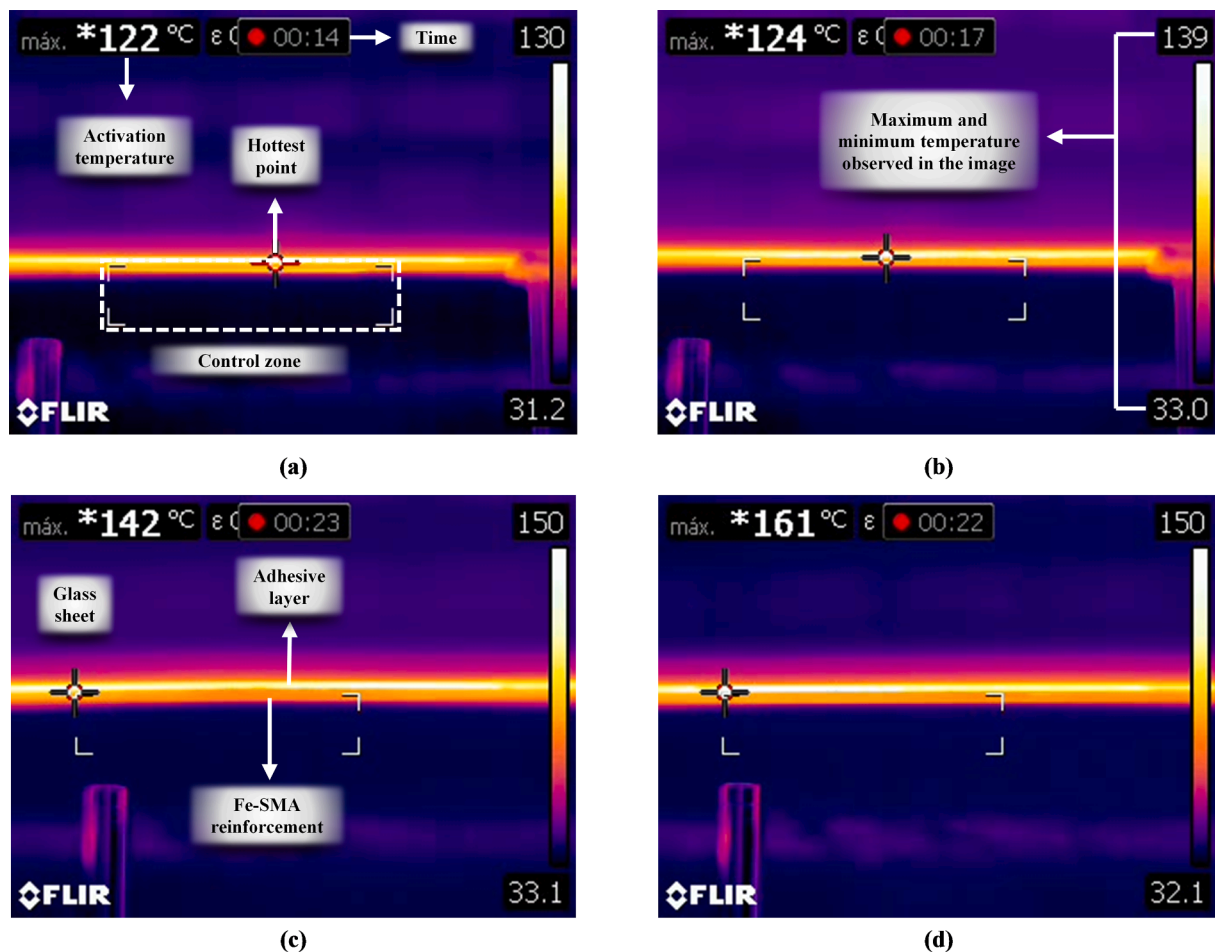
Fig. 7. Images retrieved by the infrared camera corresponding to $T = T_a$ in each of the post-tensioned beams: (a) P_T120-I, (b) P_T120-II, (c) P_T140 and (d) P_T160.

3. Activation of Fe-SMA strips

3.1. Experimental measurements

Fig. 7 shows the images captured by the infrared camera during the activation of the Fe-SMA reinforcement, when the peak temperature was reached. Fig. 8 depicts the evolution of the vertical displacement at the mid-span section (d_{exp}), the tensile strain at the top edge of the glass panel ($\varepsilon_{g,t}$) and the temperature in the Fe-SMA strip (T) during the activation process. It is noteworthy to mention that positive values correspond to tensile strains and therefore downward displacements. Finally, the values of d_{exp} and $\sigma_{g,t} = \varepsilon_{g,t} \times E_g$ registered at the end of the

Fig. 8. Activation process of the externally bonded Fe-SMA strips: displacement at mid-span (*d*), strain at the top edge of the glass panel ($\varepsilon_{g,t}$) and temperature in the Fe-SMA (*T*).

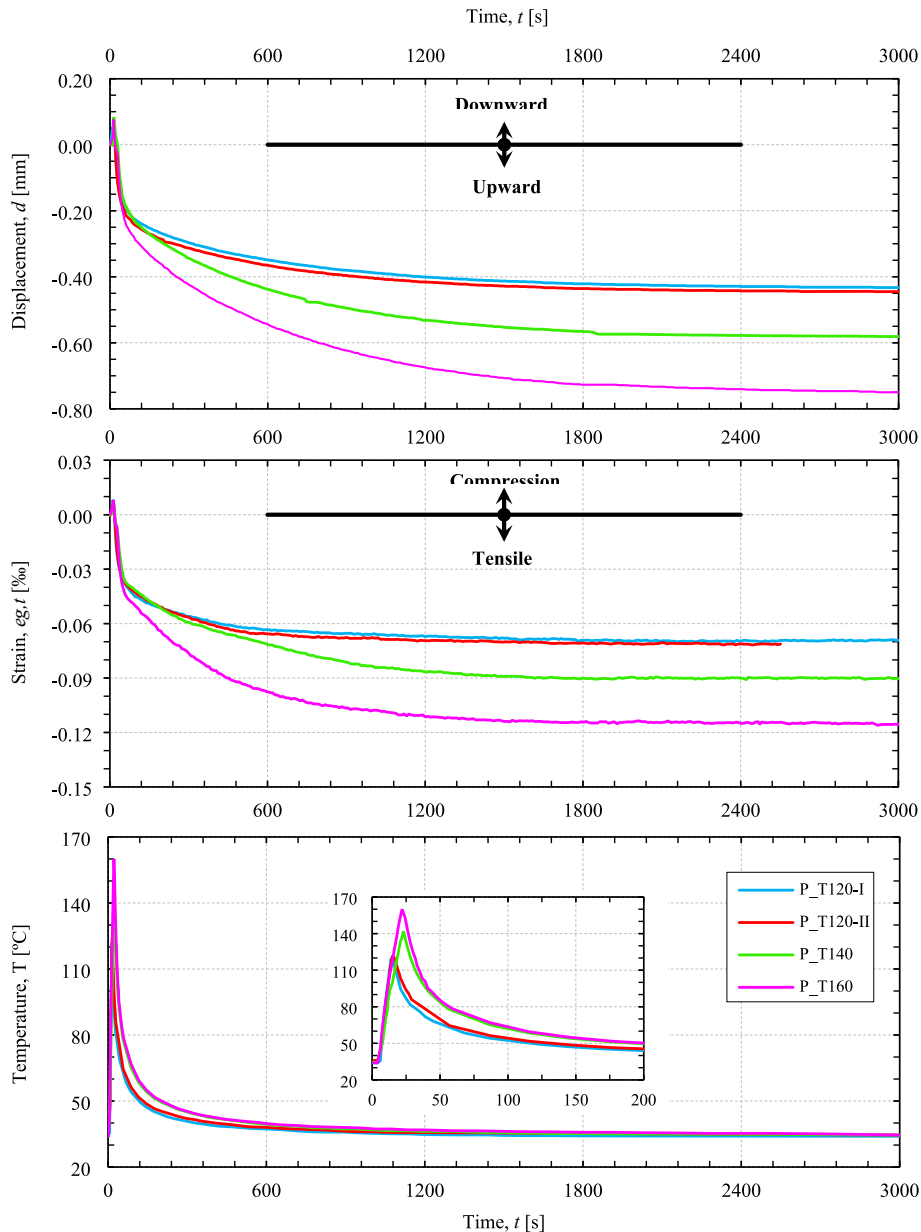cooling phase are summarized in Table 2, as well as the maximum temperature (T_a) achieved in the Fe-SMA strip. The heating phase of each beam, which lasted between 10 and 18 s, was much shorter than the subsequent cooling phase ($\approx$ 3000 s). It is noteworthy to mention that no detachment of the Fe-SMA strip from the glass substrate was observed for any of the post-tensioned beams, showing that the used adhesive performed well when exposed to the high temperatures experienced.

As shown in Fig. 8, due to the thermal expansion of the Fe-SMA strips, all beams deformed downwards between 0.067 mm and 0.086 mm at the beginning of the heating phase, leading to the appearance of compression stresses at the top region of the glass panel. A few seconds later, yet during the heating phase, these initial deformations were completely suppressed by the shape memory effect of Fe-SMAs. Due to the reverse transformation from martensite to austenite, the Fe-SMA strips developed recovery stresses and, consequently, the beams deformed upwards between 0.433 mm and 0.752 mm.

3.2. Recovery stress

Based on the strain gauge measurements, the recovery stress developed in Fe-SMA strips ($\sigma_{rec,sg}$) may be estimated by performing numerical simulations. In this study ABAQUS 6.14 finite elements software was used [56]. Both the glass and the Fe-SMA were simulated as an isotropic material with linear elastic behaviour. The mechanical properties adopted for the glass were taken from Table 1. Based on the experiments conducted by Shahverdi et al. [30], the relationship between the recovery stress (restrained Fe-SMA strip) and the recovery strain (non-restrained Fe-SMA strip) was simulated using an equivalent modulus of elasticity ($E_{r,a}$) equal to 95 GPa. In addition, within the non-activated region, the non-linear behaviour of the Fe-SMA material in tension was simulated using a USDFLD subroutine to select the modulus of elasticity as a function of the axial stress, based on the response shown in Fig. 1. A Poisson's ratio of 0.39 (see Table 1) was adopted for these numerical simulations.

Typically, polymeric adhesives do not perform well at high

Table 2

Experimental measurements retrieved from the activation of the Fe-SMA reinforcement and comparison with results extracted from numerical simulations performed to determine the recovery stress.

Experimental measurements			
Beam	T_a [°C]	d_{exp} [mm]	$\sigma_{g,t}$ [MPa]
P_T120-I	122	0.433	5.11
P_T120-II	124	0.445	5.25
P_T140	142	0.584	6.70
P_T160	161	0.752	8.51

Numerical results			
Beam	d_{num} [mm]	$\sigma_{g,b}$ [MPa]	$\sigma_{rec,sg}$ [MPa]
P_T120-I	0.412 (-4.8 %)	−10.16	201.7
P_T120-II	0.423 (-4.9 %)	−10.43	207.0
P_T140	0.539 (-7.7 %)	−13.29	263.8
P_T160	0.685 (-8.9 %)	−16.89	335.2

Notes: The values between parentheses are the difference in percentage between d_{num} and d_{exp}.

temperatures. After reaching the glass transition temperature, the polymers lose their ability to transfer shear stress between adherends. Thereby, the activation process and resulting heating effect of the Fe-SMA strips certainly reduced the shear interaction at the bonded interfaces during the activation process, and likely damaged the adhesive afterwards. A maximum working temperature of 120 °C is indicated by the adhesive's technical data sheet, but it is expectable that a considerable degradation of the mechanical properties exists at temperatures of this magnitude. Accordingly, the complete absence of shear interaction within the activated region (shaded in Fig. 5a) – no composite action – was considered in these numerical simulations. Thus, the beams were simulated by setting E_{adh} to zero in the activated length, while the remaining length of the adhesive was considered as undamaged and simulated as an isotropic material with linear elastic behaviour (E_{adh} = 1728 MPa). In the non-activated region, the numerical model assumed that the relative slippage at the reinforcement/adhesive and adhesive/glass interfaces was not possible. For the sake of simplicity, the adopted approach did not consider the thermo-mechanical behaviour of the components and neglected any heat flow into the non-activated region.

Regarding the finite element modelling, two-dimensional simulations were carried out assuming the symmetrical behaviour of the SMA reinforced glass beams with respect to the mid-span vertical axis. A finite element mesh with an element size of 5 (width) × 5 (height) [mm] was adopted, using 4-node plane stress elements (CPS4) with 2 × 2 integration points for all components. Fig. 9 shows the geometry, boundary conditions, load configuration and the mesh pattern. In addition, the rigid connection at the Fe-SMA/adhesive and adhesive/glass interfaces were materialized setting these as a "tie" constraint, which avoids relative translations and/or rotations between adjacent nodes. Recovery stresses were simulated as an imposed temperature variation along the

l_a. Finally, for each specimen, iterative numerical simulations were run until the numerical axial stress at the top edge of the glass panel attained the experimental one (see $\sigma_{g,t}$ in Table 2).

Table 2 presents the results extracted from the numerical simulations, namely the $\sigma_{rec,sg}$, the numerical displacement at the mid-span section (d_{num}) and the compression stress at the bottom edge of the glass panel ($\sigma_{g,b}$). Recovery stresses ranged between 201.7 MPa ($T_a = 120$ °C) and 335.2 MPa ($T_a = 160$ °C). As expected, beams with the lowest T_a (e.g. P_T120 beams) exhibited the lowest $\sigma_{rec,sg}$.

Concerning the beams P_T120-I and -II, d_{num} was 4.8 % to 4.9 % lower than d_{exp}, respectively. Higher differences can be found in the beams P_T140 and P_T160, where d_{num} was 7.7 % and 8.9 % lower than d_{exp}, respectively. Neglecting minor deviations in beam geometry (e.g. height), these differences seem to be related to the propagation of damage at the adhesive to the non-activated region (near the loaded end sections), which was disregarded in the numerical model. Typically, the bond behaviour of adhesively bonded connections consists of three distinct stage: (i) the elastic stage, before bond strength is attained; (ii) the softening stage, where the adhesive is still able to transfer shear stress that decreases with increasing relative slip; and (iii) the debonding stage, when there is no shear interaction between the bonded interfaces. Due to premises adopted in these numerical simulations, only the elastic (non-activated regions) and debonding (activated region) stages were modelled, respectively setting E_{adh} equal to 1728 MPa and zero. However, the underestimation of the mid-span deflection provided by the numerical model, i.e. the difference between d_{num} and d_{exp}, seems to indicate that $l_{b,d}$ – which is defined as the bond length damaged by the activation of the Fe-SMA strips – was in fact longer than l_a, even in post-tensioned specimens with the lowest activation temperature. Accordingly, it is reasonable to assume that no shear interaction exists between adherends within the activated region, providing further validation to the numerical simulations.

Adhesive damage propagation in the non-activated region was a result of the heat flow into the non-activated region, as well as the high stress concentrations at the glass-to-SMA interfaces near the loaded end sections of the non-activated Fe-SMA strip zones. As expected, the $d_{num} - d_{exp}$ relationship suggests that the adhesive damage propagation into the non-activated region was significantly influenced by the activation temperature. The application of higher T_a extended the heating phase, increasing the heat flow into the non-activated zone, and developed greater $\sigma_{rec,sg}$, increasing the stress concentrations in the anchorage zones. The combination of these two effects increased the $l_{b,d}$ and, as a consequence, the stress transfer zone between adherends shifted towards the beam ends. In practical terms, a similar effect would be obtained if a longer length of the beam was activated and post-tensioned ($l_{b,d} > l_a$), thus promoting d_{exp} slightly larger than d_{num}.

The recovery strain – recovery stress ratio depends on the restraint conditions of the anchorage zone. When assuming that the glass panel behaves as an infinitely rigid substrate, the maximum recovery stress ($\sigma_{rec,max}$) can be fully mobilized if the anchorage zones do not allow any deformation (e.g. slip at the bonded interfaces). Nevertheless, in reality,
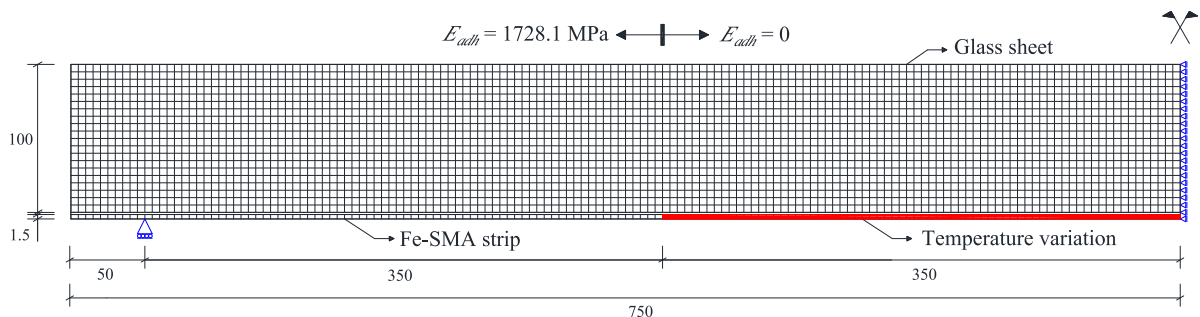

Fig. 9. Finite element model used to determine the recovery stress in the Fe-SMA strips, identifying the length (blue colour) that was subjected to temperature variation. All units in [mm]. (For interpretation of the references to colour in this figure legend, the reader is referred to the web version of this article.)

elastic deformation of the adhesive joint along the stress transfer length, as well as the adhesive damage propagation into the non-activated region (softening and debonding stages), both occur. As a consequence, the non-activated Fe-SMA strip zones located between $l_{b,d}$ and l_a were tensioned ($\sigma \approx \sigma_{rec,sg}$) and elongated. Therefore the activated Fe-SMA strip zone was allowed to contract slightly (recovery strain) and, consequently, the potential recovery stress was reduced ($\sigma_{rec,sg} \leq \sigma_{rec,max}$). Nevertheless, due to the heat flow into the non-activated region, these Fe-SMA strip zones were to some extent activated ($T < T_a$), reducing the shrinkage of the activated Fe-SMA strip zone. Therefore, it is reasonable to assume that the experimental $\sigma_{rec,sg}$ were not significantly affected by the adhesive damage propagation and resemble well the numerical ones.

The activation process was well captured when assuming no composite action between adherends within the activated region. Furthermore, it should be noted that the recovery stresses are a function of the activation temperature, the substrate stiffness and the anchorage restraint conditions. If the glass panel and the adhesive joint were infinitely stiff in flexure and shear, respectively, the $\sigma_{rec,sg}$ would have varied between 231.1 MPa ($T_a = 120\ ^\circ$C) and 379.2 MPa ($T_a = 160\ ^\circ$C), which compares very well with the values commonly found in the literature for this Fe-SMA material (e.g. [30]). Assuming $f_{g,t} = 40$ MPa (see Table 1) and neglecting its inherent variability, it would be expectable that the first cracking load of the post-tensioned beams would be 1.25 to 1.42 times higher than that obtained from R_T0 beams (increment of cracking load – ΔF_{cr}). It is noteworthy to mention that these values do not consider any influence of the activation procedure on the mechanical properties of the Fe-SMA reinforcement.

4. Results and discussion

Fig. 10 and Figs. 11–12 show the applied load (F) *versus* mid-span deflection (δ) experimental responses of the reference and post-tensioned beams, respectively, as well as the crack patterns obtained using the DIC technique at different stages. On the other hand, Table 3 summarizes the experimental responses in terms of initial stiffness (K), cracking load (F_{cr}) and corresponding deflection (δ_{cr}), maximum load (F_{max}), and ultimate deflection (δ_{ult}). Table 3 lists two additional parameters: (i) the residual strength index (RSi), which was defined as the F_{max} / F_{cr} ratio, quantifying the load carrying capacity after crack initiation; and (ii) the ductility index at failure (Di), which was defined as the $\delta_{ult} / \delta_{cr}$ ratio, quantifying the capacity of the beams to deform after the appearance of the first crack.

4.1. Reference beams

As shown in Fig. 10, both reference beams presented similar structural responses, exhibiting linear behaviour during the pre-cracking stage with $K = 1.53$ kN/mm. Thereafter, successive sudden load drops occurred due to the appearance of cracks appearing from the mid-span section towards the supports, creating non-linear branches with progressive loss of stiffness due to the yielding of the Fe-SMA. The large crack openings attained and the extensive horizontal crack propagation generated crack branching (V-shaped cracks). The high deformation capacity of the reinforcement material delayed the appearance of shear cracks, as well as the debonding of the Fe-SMA strip. The R_T0-I beam failed due to debonding of the Fe-SMA strip at the reinforcement/adhesive interface (see Fig. 13) due to cracks that formed in the shear span (failure mode: critical shear crack). In contrast, the R_T0-II beam was unloaded prior to collapse because the maximum deflection allowed by
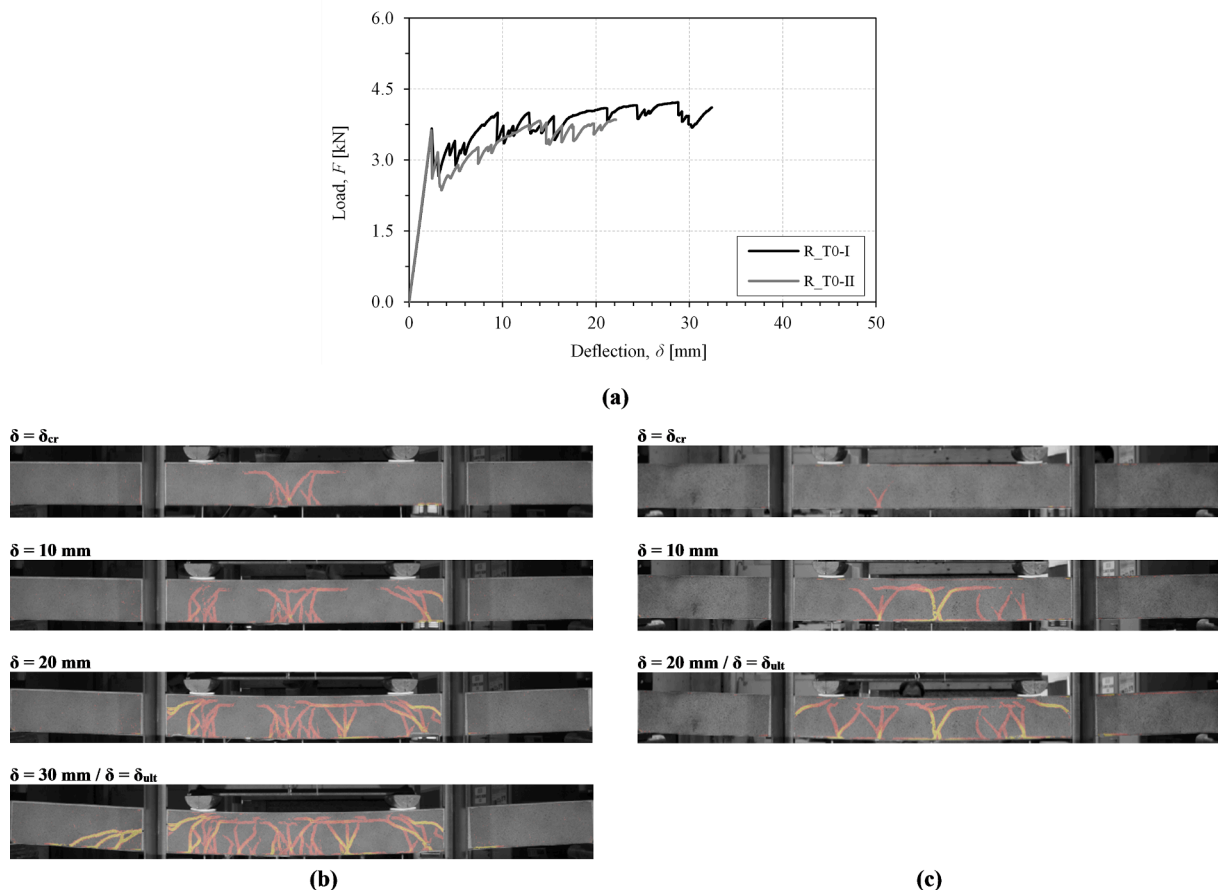

(a)

(b)

(c)

Fig. 10. Results of the flexural tests with the reference beams: (a) structural responses and crack patterns of the beams (b) R_T0-I and (c) R_T0-II at different stages.
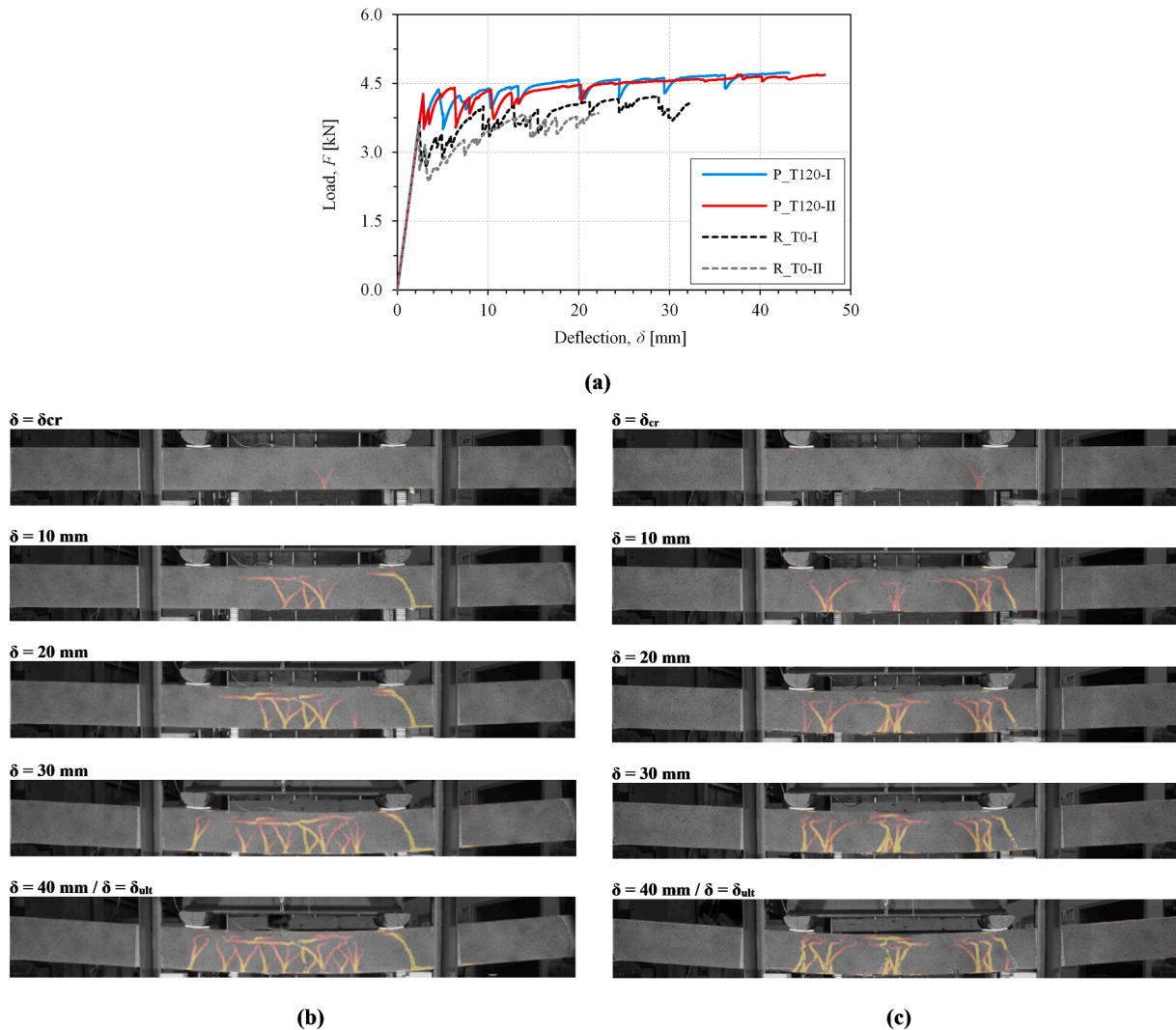
(a)

(b)

(c)

Fig. 11. Results of the flexural tests with the post-tensioned beams: (a) comparison between the structural responses of both P_T120 beams with those of the reference series, as well as the crack pattern of the beams (c) P_T120-I (c) and (d) P_T120-II at different stages.

the experimental setup was reached. In general, both R_T0 beams showed the ability to recover the load carrying capacity after initial cracking, exceeding F_{cr} during the post-cracking stage. These results show that glass structural elements can present safe and ductile responses when Fe-SMA is used as reinforcement, as previously observed by Silvestru *et al.* [48].

4.2. Post-tensioned beams

4.2.1. Initial stiffness

Similarly to the reference beams, all post-tensioned beams exhibited linear behaviour during the pre-cracking stage. Excluding the P_T160 beam, all post-tensioned beams showed lower initial stiffness than the reference beams, between 1.8 % (P_T120-I beam) and 2.7 % (P_T140 beam). This reduction is explained by two main aspects: (i) first, heating the Fe-SMA strips partially damaged the adhesive joint of post-tensioned beams, reducing the composite action between adherends; and (ii) second, the tensile stiffness of the Fe-SMA strips decreased after activation [30]. Thereby, the reduction of the initial stiffness of post-tensioned beams showed to be proportional to T_a. Unexpectedly, the P_T160 beam showed the highest initial stiffness among the post-tensioned beams, being 0.7 % higher than the one obtained from the R_T0 series. This can be explained by minor geometric deviations, as well as

residual frictional forces between the glass panel and the lateral guides.

4.2.2. First cracking load

When comparing the post-tensioned beams with the R_T0 series, it is possible to observe that the activation of the Fe-SMA reinforcement increased the glass fracture strength between 16.8 % – in the P_T120-I beam (with the lowest T_a) – and 30.3 % – in the P_T160 beam (with the highest T_a). According to Table 3, the first cracking loads obtained from bending tests (F_{cr} (P_T120-I beam) < F_{cr} (P_T120-II beam) < F_{cr} (P_T140 beam) < F_{cr} (P_T160 beam) are consistent with the results obtained from the activation process. However, the estimated ΔF_{cr} for post-tensioned beams (see Section 3.2) were not reached, being the experimental ΔF_{cr} (see Table 3) between 6.8 % (P_T120-I beam) and 8.4 % (P_T140 beam) lower than the former. Despite the inherent variability of the tensile strength of glass, as well as the decrease in tensile stiffness of the Fe-SMA material after activation (see Section 4.2.1), the loss of post-tensioning force (stress relaxation in Fe-SMA) seems to be the main explanation for this difference, as observed in previous studies on the long term-behaviour of activated Fe-SMA reinforcement (e.g. [30,41]).

Based on the F_{cr} obtained from flexural tests, the analytical model presented in Appendix A was used to determine the decrease in post-tensioning force over time, assuming linear elastic behaviour for all components, as well as the strain distribution shown in Fig. 14. Based on
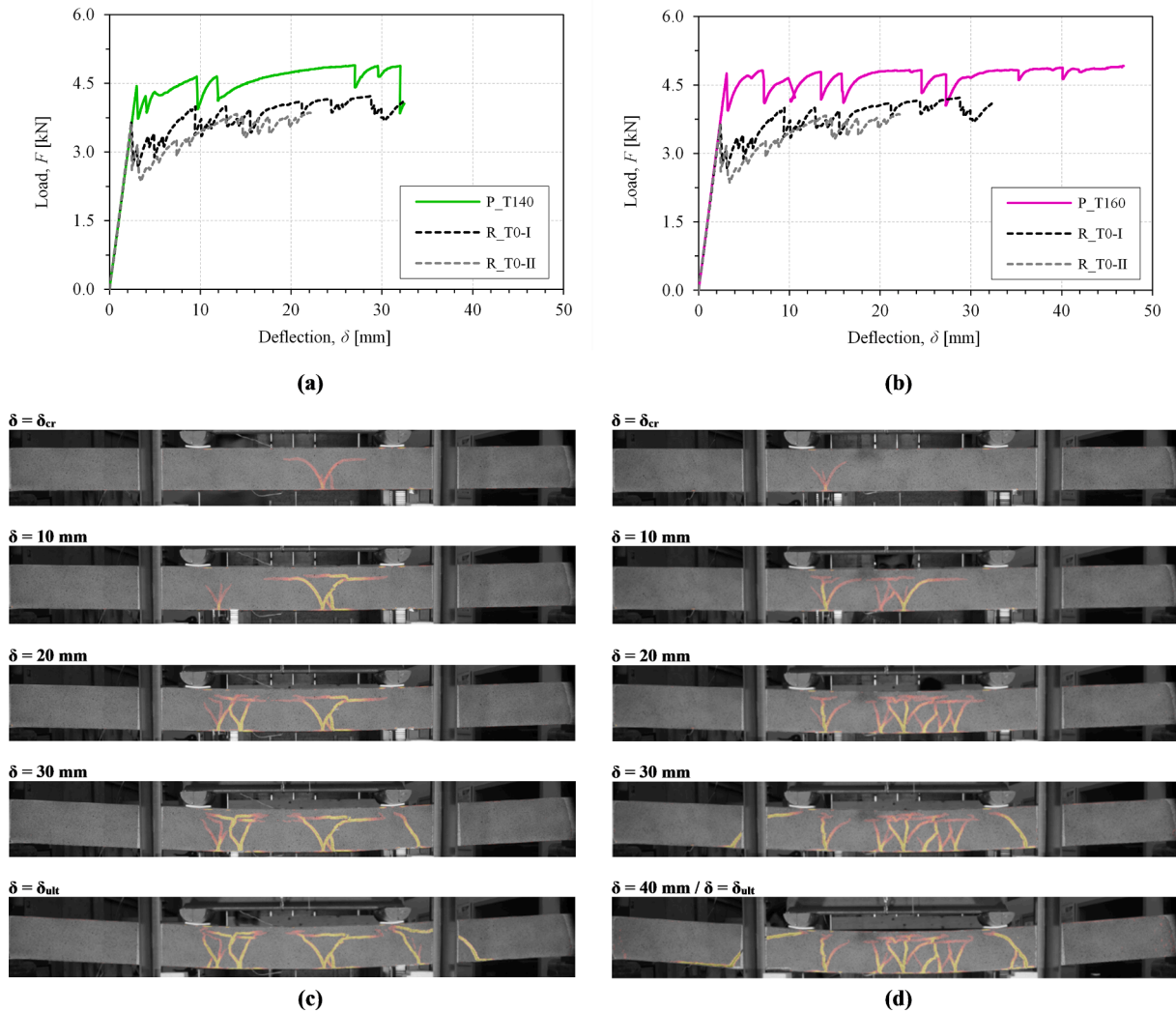
Fig. 12. Results of the flexural tests with the post-tensioned beams: comparison between the structural responses of the beams (a) P_T140 and (b) P_T160 and those obtained from the reference series, as well as the crack pattern of the beams (c) P_T140 and (d) P_T160 at different stages.

previous studies (e.g. [28,29]), the stress – strain curve shown by activated Fe-SMA strips resembles the one shown by passive Fe-SMA strips after the former achieve an increase in axial strain (ε_{rev}) of ∼ 1.0 % (see Fig. 2). Thus, the reversal stress (σ_{rev}) was assumed equal to $\sigma(\varepsilon_{pre}) = 638.5$ MPa (maximum stress reached during the pre-straining process).

Table 4 compares the recovery stresses obtained from cracking loads ($\sigma_{rec,cr}$) and strain gauges measurements ($\sigma_{rec,sg}$). Values of $\sigma_{rec,cr}$ lower than $\sigma_{rec,sg}$ were obtained in all beams, varying between 4.9 % (P_T120-I beam) and 10.1 % (P_T140 beam). It is noteworthy to mention that, for the sake of simplicity, the analytical procedure did not take into account several aspects that obviously influenced the first cracking load of post-tensioned beams, mainly the permanent adhesive damage after the activation of the Fe-SMA strips and its effect on the composite action reduction. According to Eq. (A.8) in Appendix A, lower values of I_{el} would result in higher recovery stresses. Therefore, if the adhesive damage would have been introduced in the analytical procedure, the difference between $\sigma_{rec,cr}$ and $\sigma_{rec,sg}$ would be smaller, mainly in the beams whose Fe-SMA strips were activated at higher temperatures.

Disregarding small temperature variations, which may have slightly reduced the post-tensioning force due to the thermal expansion of the Fe-SMA reinforcement, the stress relaxation of Fe-SMA material is the main explanation for why the $\sigma_{rec,cr}$ were consistently lower than the $\sigma_{rec,sg}$. The post-tensioned beams were tested up to 48 h after activation of the Fe-SMA strips. According to the tensile relaxation tests conducted by

Shahverdi et al. [30], activated Fe-SMA strips with an initial recovery stress of 350 MPa ($\approx \sigma_{rec,sg}$ for the P_T160 beam) experienced a relaxation of ∼ 6.0 % during this time period. It should be noted that the relaxation behaviour depends on the amount of recovery stress and, in line with the experimental results, stress relaxation in Fe-SMA increases for increasing recovery stress. Nevertheless, according to Hosseini et al. [53], a significant part of the losses in the recovery stress can be retrieved by reactivating the Fe-SMA reinforcement, providing a possible solution to restore the initial recovery stresses in practical applications.

4.2.3. Post-cracking behaviour

In general, the post-cracking behaviour is characterized by a series of sudden load drops which create non-linear branches, with progressive loss of stiffness due to the martensitic transformation in the Fe-SMA reinforcement (see Figs. 11 and 12). Like in the R_T0 series, crack propagation towards the supports was delayed by the extremely ductile behaviour of the Fe-SMA after the martensitic transformation. The post-tensioned beams presented high deformation capacity, reaching ductility values above 1000 %. In terms of residual strength, all post-tensioned beams were able to exceed the first cracking load during the post-cracking stage.

Compared to the R_T0 series, the post-tensioned beams achieved higher values of F_{max}, between 16.2 % (P_T120-I beam) and 21.7 %

Table 3
Main properties of the reference (R_T0) and post-tensioned (P_T120, P_T140 and P_T160) SMA reinforced glass beams extracted from the flexural tests.

Reference beams

Property	R_T0-I	R_T0-II	R_T0 series
K [kN/mm]	1.53	1.53	1.53
F_{cr} [kN]	3.67	3.63	3.65
δ_{cr} [mm]	2.40	2.38	2.39
F_{max} [kN]	4.22	3.86	4.04
δ_{ult} [mm]	32.9	22.1	27.5
Di [%]	1370	931	1151
RSi [%]	115	106	111

Post-tensioned beams

Property	P_T120-I	P_T120-II	P_T140	P_T160
T_a [°C]	122	124	142	161
K [kN/mm]	1.50 (-1.8 %)	1.50 (-1.9 %)	1.49 (-2.7 %)	1.54 (0.7 %)
F_{cr} [kN]	4.26 (16.8 %)	4.28 (17.2 %)	4.44 (21.8 %)	4.75 (30.3 %)
δ_{cr} [mm]	2.84 (19.0 %)	2.86 (19.5 %)	2.99 (25.2 %)	3.09 (29.5 %)
F_{max} [kN]	4.74 (17.2 %)	4.69 (16.2 %)	4.89 (21.1 %)	4.92 (21.7 %)
δ_{ult} [mm]	43.2 (56.8 %)	47.1 (71.0 %)	32.5 (17.8 %)	46.8 (70.0 %)
Di [%]	1519 (31.9 %)	1648 (43.2 %)	1085 (-5.7 %)	1512 (31.5 %)
RSi [%]	111 (0.4 %)	110 (-0.8 %)	110 (-0.6 %)	103 (-6.6 %)

Notes: The values indicated in parentheses represents the difference between the property of the post-tensioned beams with the one of the reference beams.

(P_T160 beam). However, in general, the post-tensioned beams showed lower RSi values than the reference ones. The activation of the Fe-SMA reinforcement reduced its tensile strength reserve (difference between σ_{rev} and $\sigma_{rec,sg}$) before the forward transformation, thus reducing significantly the post-cracking stiffness of the post-tensioned beams, as well as their load carrying capacity. Therefore, as experimentally observed, the residual strength tended to be lower in beams with higher T_a. Nevertheless, the P_T140 beam displayed an unexpectedly high RSi value among the post-tensioned beams. The high scatter of the tensile strength of glass seems to be the main reason for this result, having produced a lower F_{cr} than expected. This also justifies why the P_T140 beam showed a greater difference between $\sigma_{rec,cr}$ and $\sigma_{rec,sg}$ (see Section 4.2.2) than the P_T160 beam.

Glass structures are safe only when the resisting mechanism generated after the initial glass cracking is capable of assuring a load carrying capacity that is higher than the F_{cr}. Therefore, a maximum recovery stress ($\sigma_{rec,max}$) should be estimated to ensure $F_{ult} > F_{cr}$. After cracking, the load carrying mechanism is formed by a compression force in the uncracked glass zone and a tensile force in the reinforcement element, identified as $F_{c,g}$ and $F_{t,r}$ in Fig. 15, respectively. Two failure mechanism were considered: (i) tensile failure in the Fe-SMA reinforcement and (ii) crushing of the cross-section area where compression stresses are maximum. Lateral instability and debonding of the Fe-SMA strip were neglected because they can be postponed or avoided by changing the beam geometry and choosing adhesives with greater shear resistance, respectively. The compression strength of glass ($f_{g,c}$) was not experimentally characterized in this investigation. A $f_{g,c} = 500$ MPa was adopted in this study [57].

Based on Appendix B, the maximum recovery stress obtained when the beam collapse is governed by glass crushing and tensile failure in Fe-SMA is equal to 379.7 MPa and 612.4 MPa, respectively (see Table 5). Considering the lowest value, F_{cr} ($\sigma_{rec,max} = 379.7$ MPa) is equal to 5.07 kN, which represents a maximum increment of ~ 40.0 % in cracking load taking the R_T0 series as a reference. In any case, the recovery stress – activation temperature relationship reaches a maximum for which an

increase in temperature no longer results in an increase in the recovery stress, which according to Shahverdi *et al.* [30] is equal to approximately 450 MPa. As discussed in Section 4.2.2, the recovery stress reduces over time due to stress relaxation of the Fe-SMA material. Therefore, recovery stresses slightly higher than $\sigma_{rec,max}$ can be introduced. However, further investigation to determine the amount of stress relaxation over time is particularly important.

4.2.4. Failure modes

Excluding the P_T140 beam, which failed due to debonding of the Fe-SMA strip at the reinforcement/adhesive interface (see Fig. 13a), all post-tensioned beams were unloaded before collapse when the maximum deformation allowed by the experimental setup was exceeded. In the P_T140 beam, the detachment of the Fe-SMA strip was triggered by a critical shear crack that appeared in the non-activated region. Due to the low fracture energy of glass, strain energy is suddenly released during the crack formation, damaging the adhesive joint around the crack. Then, shear cracks induce high interfacial stresses (mode-I and -II) at the bonded interfaces, causing progressive debonding of the reinforcement.

Fig. 13b shows a close up of the partial detachment of the Fe-SMA strip observed in the post-tensioned beams after unloading, which seems to have resulted from the cohesive failure of the adhesive used. Nevertheless, the adhesive was able to keep the reinforcement bonded to the glass, probably because shear cracks did not appear sufficiently close to the supports, as occurred in the case of the P_T140 beam. Therefore, further investigation is necessary to understand in detail this failure mechanism and to develop an analytical model to predict the collapse due to critical shear crack in passive and post-tensioned composite glass systems.

5. Conclusions

This research was focused on the structural performance of post-tensioned glass beams using Fe-SMA as reinforcement. First, Fe-SMA strips were mechanically deformed to induce the martensitic transformation. Second, pre-strained Fe-SMA strips were adhesively bonded to the bottom edge of glass panels using an epoxy adhesive. Third, the Fe-SMA strips were activated by resistive heating at temperatures between 120 °C and 160 °C, approximately. Finally, the post-tensioned beams were experimentally tested until failure under a four-point bending configuration. In addition, based on the strain gauge measurements, numerical investigations were performed to determine the initial stress-state generated by the activation of Fe-SMA strips.

The main conclusions of this research may be summarized as follows:

- Post-tensioning of glass beams by activating Fe-SMA strips adhesively bonded is a relatively quick and easy process. Partial activation of Fe-SMA strips proved to be a suitable strategy to avoid the concentration of high shear stresses in weaker zones of the glass panel (e.g. beam ends), ensuring an undamaged bond region able to transfer the post-tensioning force from the reinforcement element to the glass substrate;
- Numerical models showed that the loss of composite action was directly correlated to the activation temperature; higher activation temperature resulted smoother post-tensioning force transfer, significantly reducing the possibility of premature glass breakage. In addition, the propagation of adhesive damage into the non-activated region increased the vertical displacement at the mid-span section;
- Four-point bending tests proved the feasibly of SMA strengthening of glass beams. All beams were able to maintain their integrity during the cracking process, exhibiting a post-cracking behaviour that was strongly influenced by the mechanical properties of the adhesive and reinforcement. Relatively safe and ductile failure mechanisms were achieved in the strengthened glass beams;
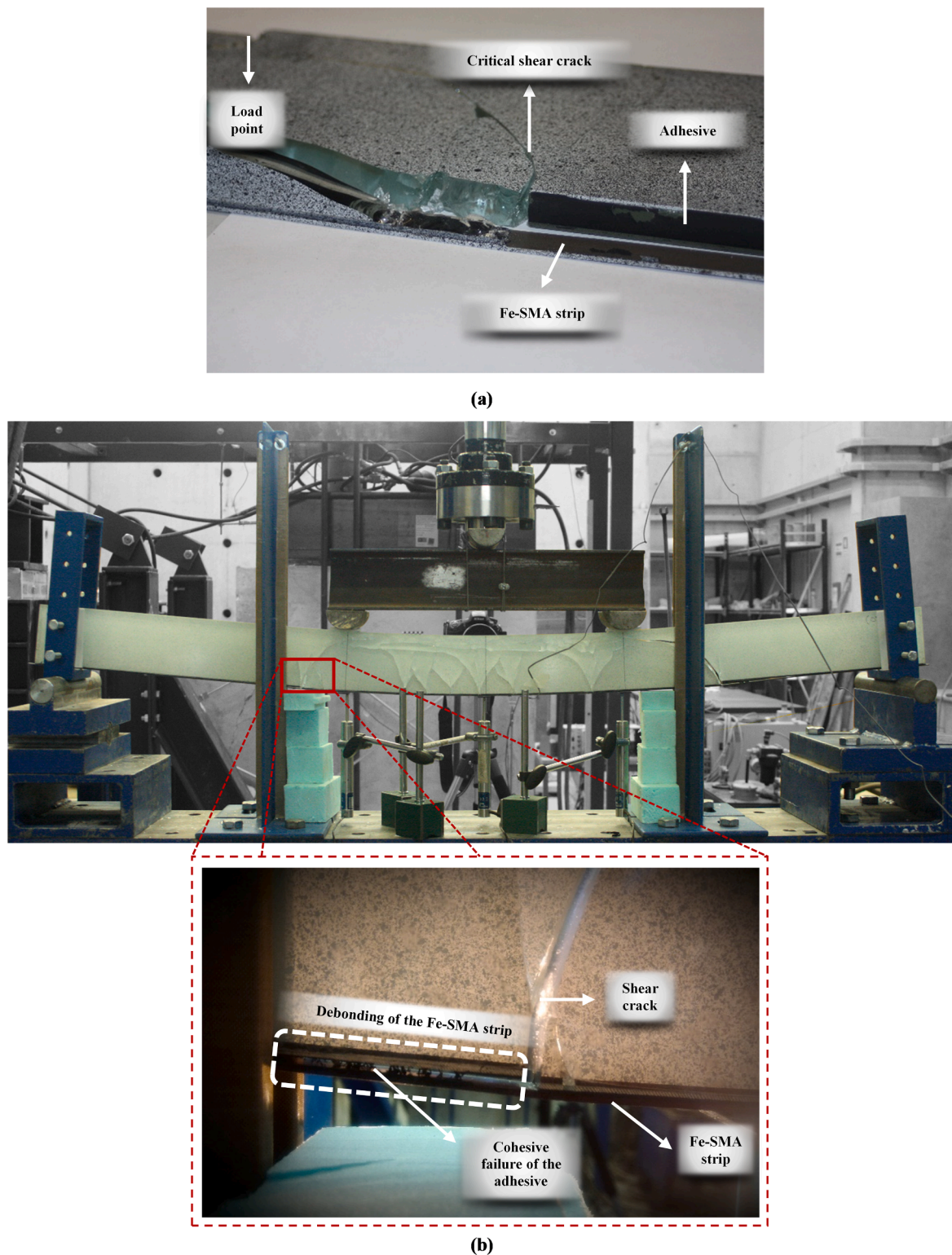
(a)

(b)

Fig. 13. Failure modes: (a) debonding of the Fe-SMA strip at the adhesive/reinforcement interface observed in the beams R_T0-II and P_T140; and (b) cohesive failure of the 3 M adhesive due to the appearance of shear cracks.

- In general, the activation of the Fe-SMA strips was an advantageous strategy to enhance the overall response of glass composite systems. The post-tensioning resulted in first cracking loads ranging between 17 % and 30 % higher than those obtained with reference beams (passive Fe-SMA reinforcement);
- Due to the stress relaxation behaviour of the Fe-SMA, the post-tensioning stress decreased over time between 4.9 % and 10.1 %,

depending on the recovery stress. However, for practical applications, the initial recovery stresses could be retrieved by reactivating the Fe-SMA reinforcement;
- All beams were able to exceed the first cracking load during the post-cracking stage. The post-cracking behaviour of the post-tensioned beams was mainly influenced by the recovery stress developed in Fe-SMA strips. Compared to the reference beams, the post-tensioned
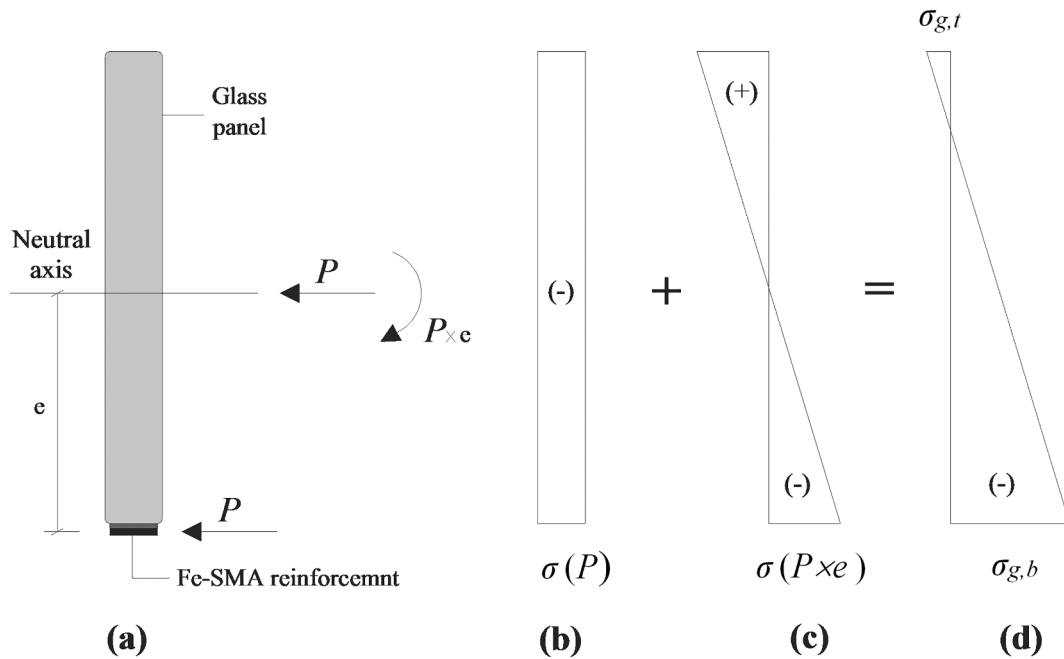
Fig. 14. Stress distribution due to the post-tensioning: (a) compression and flexural forces; (b) compression stress and (c) flexural stress distributions; and (d) final stress distribution.

Table 4
Parameters used to determine the recovery stresses from cracking loads and comparison with the ones derived from the strain gauges measurements.

Beam	I_{el} [mm^4]	I_a [mm^4]	$\sigma_{rec,sg}$ [MPa] [a]	$\sigma_{rec,cr}$ [MPa]
P_T120-I	973645.3	951294.1	201.7	191.8 (-4.9 %)
P_T120-II	973386.9		207.0	195.3 (-5.6 %)
P_T140	970587.7		263.8	237.3 (-10.1 %)
P_T160	967071.0		335.2	313.4 (-6.5 %)

Notes: [a] Values retrieved from Table 2 considering no composite action between adherends. Post-tensioning force loss is indicated in parentheses and represents the difference between $\sigma_{rec,cr}$ and $\sigma_{rec,sg}$.
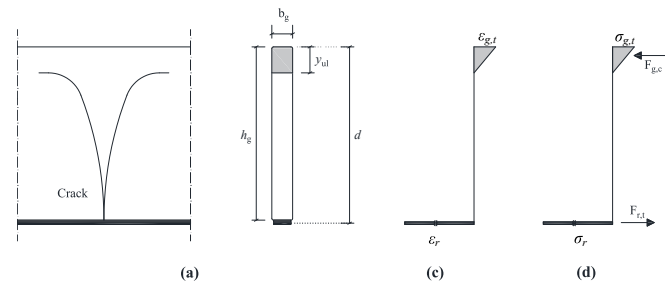
Table 5
Main parameters used to determine the maximum recovery stress that guarantees the safe collapse of composite beams.

Fe-SMA tensile failure				
ε_r [‰]	$\sigma_{g,t}$ [MPa]	y_{ult} [mm]	$\sigma_{rec,max}$ [MPa]	$F_{cr} = F_{ult}$ [kN]
324.9	$755.8 > f_{g,c}$	3.20	612.4	5.99

Glass crushing				
ε_r [‰]	$\sigma_{g,t}$ [MPa]	y_{ult} [mm]	$\sigma_{rec,max}$ [MPa]	$F_{cr} = F_{ult}$ [kN]
$174.3 < \varepsilon_{r,ult}$	500.0	4.02	379.7	5.07

Fig. 15. Resistant mechanism after glass cracking: (a) and (b) cracked cross-section and (c) strain and (d) stress distributions.

beams showed lower residual strength indexes for increasing activation temperatures, since the activation of the Fe-SMA strips reduced the tensile strength reserve before the austenite–martensite transformation;

- In order to avoid catastrophic collapses, it is recommendable that a maximum recovery stress is not exceeded so that the ultimate load is at least equal to the first cracking load, considering all possible failure mechanisms.

The results obtained from the experimental tests showed that the post-tensioning of annealed glass beams using adhesively bonded Fe-

SMA strips is a feasible and promising strengthening strategy, capable of generating safe and ductile failure mechanisms. However, additional investigation is required to address aspects that can promote post-tensioning losses over time, whether related to the post-tensioning procedure (e.g. structural performance of glass-to-SMA adhesive joints at high temperatures and adhesive damage propagation) or long-term behaviour (e.g. relaxation behaviour of the Fe-SMA, creep in the adhesive joint due to permanent shear stresses imposed by the post-tensioning). In addition, the effect of different environmental conditions (e.g. temperature, moisture and UV radiation) should also be considered in future studies. As glass is a transparent material, special attention should be paid to the influence of the solar radiation, especially the UV radiation and thermal cycling, on the bond behaviour of adhesive connections over time. Thus, in order to promote the use of Fe-SMA reinforced glass elements in a wide spectrum of applications, additional experimental studies should focus on the aspects mentioned above, as well as on the development of reliable analytical/numerical methodologies to simulate the activation procedure (e.g. thermo-mechanical analysis) and predict the structural response of post-tensioned glass-SMA composite systems.

CRediT authorship contribution statement

Jorge Rocha: Investigation, Writing – original draft. **Eduardo Pereira:** Conceptualization, Methodology, Writing – review & editing, Supervision, Resources. **José Sena-Cruz:** Methodology, Validation, Writing – review & editing, Supervision, Resources.

Declaration of Competing Interest

The authors declare that they have no known competing financial interests or personal relationships that could have appeared to influence the work reported in this paper.

Data availability

Data will be made available on request.

Appendix A

The recovery stress ($\sigma_{rec,cr}$) can be derived from the first cracking load. For the sake of simplicity, the tensile behaviour of activated Fe-SMA strips was assumed to be bilinear (see Fig. 2), with the first branch including $\varepsilon \leq \varepsilon_{rev}$ and the second $\varepsilon > \varepsilon_{rev}$. An equivalent modulus of elasticity ($E_{r,rec}$), defined as the slope of the first linear branch (see Eq. (A.1)), was conservatively used in these calculations.

$$E_{r,rec} = (\sigma_{rev} - \sigma_{rec})/\varepsilon_{rev} \tag{A.1}$$

Neglecting the adhesive damage, the moment of inertia (I_{el}) is given by Eq. (A.2), in which b_i, h_i and E_i correspond to the width, height and modulus of elasticity of each component, and z_i determines the distance between the centroid and the neutral axis. In turn, the position of neutral axis (y_{el}) can be determined by means of Eq. (A.3), where $z_{i,t}$ represents the distance between the centroid of each component and the beam's top edge.

$$I_{el} = \sum \left(\frac{b_i h_i^3}{12} \cdot \frac{E_i}{E_g} + b_i h_i z_i^2 \cdot \frac{E_i}{E_g} \right) \tag{A.2}$$

$$y_{el} = \frac{\sum b_i h_i z_{i,t} \cdot E_i/E_g}{\sum b_i h_i \cdot E_i/E_g} \tag{A.3}$$

Cracking initiates when $f_{g,t}$ is attained at the bottom edge of the glass panel. Therefore, the initial compression stress at the bottom edge of the glass panel ($\sigma_{g,b}$) can be determined from Eq. (A.4), where F_{cr} is the cracking load, l_1 is the length of the shear span and h_g is the height of the glass panel.

$$\sigma_{g,b} = \frac{F_{cr} l_1}{2 I_{el}} \cdot (h_g - y_{el}) - f_{g,t} \tag{A.4}$$

Considering Fig. 14, $\sigma_{g,b}$ can be written as a function of $\sigma_{rec,cr}$ using Eq. (A.5), in which A_r is the cross-section area of the Fe-SMA strip, d is the distance between the intermediate fibre of the Fe-SMA strip and the top glass edge, and A_a is the cross-section area of the composite beam. I_a and A_a are given by Eqs. (A.6) and (A.7), respectively, while y_a can be determined through Eq. (A.3), like y_{el}, but in this case considering only the contribution of the glass panel and the Fe-SMA strip (no composite action). According to Section 3.2, these parameters were calculated assuming $E_{r,a} = 95$ GPa and $E_{adh} = 0$.

$$\sigma_{g,b} = \frac{\sigma_{rec,cr} \cdot A_r}{A_a} + \frac{\sigma_{rec,cr} \cdot A_r \cdot (d - y_a)}{I_a} \cdot (h_g - y_a) \tag{A.5}$$

$$I_a = \sum \left(\frac{b_i h_i^3}{12} \cdot \frac{E_i}{E_g} \right) \tag{A.6}$$

$$A_a = \sum b_i h_i \cdot E_i/E_g \tag{A.7}$$

Finally, equating Eqs. (A.4) and (A.5), $\sigma_{rec,cr}$ can be determined as a function of F_{cr} using the following expression:

$$\sigma_{rec,cr} = \left(\frac{F_{cr} \cdot l_1}{2 I_{el}} (h_g - y_{el}) - f_{g,t} \right) \Big/ J$$

where,

$$J = \left(\frac{A_r}{A_a} + \frac{A_r \cdot (d - y_a)}{I_a} \cdot (h_g - y_a) \right) \tag{A.8}$$

Appendix B

Tensile failure in Fe-SMA

Considering the strain distribution shown in Fig. 15, the beam collapse is governed by Eq. (B.1), in which $\varepsilon_{g,t}$ is the axial strain at the top edge of glass and y_{ult} represents the position of the neutral axis at failure.

$$\varepsilon_{g,t} = \frac{(\varepsilon_{r,ult} - \varepsilon_{rem}) \cdot y_{utl}}{(d - y_{ult})} \leqslant \frac{f_{g,c}}{E_g} \tag{B.1}$$

With,

$$y_{ult} = \frac{2 A_r \cdot f_{r,t}}{t \cdot \varepsilon_{g,t} \cdot E_g}$$

By enforcing the equilibrium of internal forces, the ultimate load (F_{ult}) is provided by Eq. (B.2).

$$F_{ult} = \frac{2 \cdot A_r \cdot f_{r,t} \cdot (d - y_{ult}/3)}{l_1} \tag{B.2}$$

From the rearrangement of Eq. (A.8), F_{cr} can be determined from Eq. (B.3).

$$F_{cr} = \frac{2 I_{el}}{(h_g - y_{el}) \cdot l_1} \cdot (J \cdot \sigma_{rec,\max} + f_{g,t}) \tag{B.3}$$

No composite action between the adherends was considered to determine I_a and A_a (see Section 3.2). Thereby, equating Eqs. (B.2) and (B.3), $\sigma_{rec,\max}$ can be calculated through the following expression:

$$\sigma_{rec,\ \max} \leqslant \frac{A_r \cdot f_{r,t} \cdot (d - y_{ult}/3) \cdot (h_g - y_{el})}{J \cdot I_{el}} - \frac{f_{g,t}}{J} \tag{B.4}$$

Glass crushing

Assuming glass crushing, the tensile strain in the Fe-SMA strip (ε_r) at failure is given by Eq. (B.5), considering by default $\varepsilon_r > \varepsilon_{rem} + \varepsilon_{rev}$.

$$\varepsilon_r = \frac{f_{g,c} \cdot (d - y_{ult})}{E_g \cdot y_{ult}} + \varepsilon_{rem} \leqslant \varepsilon_{r,ult} \tag{B.5}$$

With,

$$y_{ult} = \frac{2 A_r \cdot (\sigma_{rev} + (\varepsilon_r - \varepsilon_{rem} - \varepsilon_{rev}) \cdot E_{r,rev})}{t \cdot f_{g,c}}$$

F_{ul} is given by the following expression:

$$F_{ul} = \frac{t \cdot f_{g,c} \cdot y_{ult} \cdot (d - y_{ult}/3)}{l_1} \tag{B.6}$$

In order to determine $\sigma_{rec,\max}$ corresponding to the glass crushing, Eqs. (B.3) and (B.6) were equated and Eq. (B.7) was obtained.

$$\sigma_{rec,\max} \leqslant \frac{t \cdot f_{g,c} \cdot y_{ult} \cdot (d - y_{ult}/3) \cdot (h_g - y_{el})}{2 I_{el} \cdot J} - \frac{f_{g,t}}{J} \tag{B.7}$$

References

[1] D. Yankelevsky, Strength prediction of annealed glass plates - A new model, Engineering Structures 79 (2014) 244–255, https://doi.org/10.1016/j.engstruct.2014.08.017.

[2] F. Veer, Y. Rodichev, The structural strength of glass: Hidden damage, Strength of Materials 43 (2011) 302–315, https://doi.org/10.1007/s11223-011-9298-5.

[3] M. Haldimann, A. Luible, M. Overend, Structural use of glass, LABSE - Lanka Association of Building Services Engineers (2008).

[4] L. Biolzi, M. Orlando, L.R. Piscitelli, P. Spinelli, Static and dynamic response of progressively damaged ionoplast laminated glass beams, Composite Structures 157 (2016) 337–347, https://doi.org/10.1016/j.compstruct.2016.09.004.

[5] J. Correia, L. Valarinho, F. Branco, Post-cracking strength and ductility of glass-GFRP composite beams, Composite Structures 93 (2011) 2299–2309.

[6] P. Cruz, J. Pequeno, Structural Timber-Glass Adhesive Bonding. Challenging, Glass (2008) 205–214.

[7] P. Cruz, J. Pequeno. Timber-Glass Composite Beams: Mechanical Behaviour & Architectural Solutions. Challenging Glass, 2008, p. 439–48.

[8] J. Belis, D. Callewaert, D. Delincé, I.R. Van, Experimental failure investigation of a hybrid glass / steel beam, Engineering Failure Analysis 16 (2009) 1163–1173, https://doi.org/10.1016/j.engfailanal.2008.07.011.

[9] F. Bos, F. Veer, G. Hobbelman, C. Louter. Stainless steel reinforced and post-tensioned glass beams. ICEM12 - 12th International Conference on Experimental Mechanics, Bari, Italy: 2004, p. 1–9.

[10] C. Louter, J. Belis, F. Veer, J. Lebet, Structural response of SG-laminated reinforced glass beams; experimental investigations on the effects of glass type, reinforcement percentage and beam size, Engineering Structures 36 (2012) 292–301, https://doi.org/10.1016/j.engstruct.2011.12.016.

[11] C. Louter, J. Cupać, J. Lebet, Exploratory experimental investigations on post-tensioned structural glass beams, Journal of Facade Design and Engineering 2 (2014) 3–18, https://doi.org/10.3233/FDE-130012.

[12] C.Louter, J. Cupać, M. Debonnaire. Structural glass beams prestressed by externally bonded tendons. GlassCon Global Conference Proceedings, Philadelphia, EUA: 2014, p. 450–9, https://doi.org/10.14296/deeslr.v5i0.1848.

[13] M. Palumbo, A New Roof for the XIIIth Century 'Loggia de Vicari` (Arquà Petrarca – PD Italy) Based on Structural Glass Trusses: A Case Study, Glass Processing Days, Tempere, Finland, 2005.

[14] J. Rocha, J. Sena-Cruz, E. Pereira, Influence of adhesive stiffness on the post-cracking behaviour of CFRP-reinforced structural glass beams, Composites Part B: Engineering 110293 (2022), https://doi.org/10.1016/j.compositesb.2022.110293.

[15] M. Achintha, B. Balan, Characterisation of the mechanical behaviour of annealed glass – GFRP hybrid beams, Construction and Building Materials 147 (2017) 174–184, https://doi.org/10.1016/j.conbuildmat.2017.04.086.

[16] C. Bedon, C. Louter, Numerical investigation on structural glass beams with GFRP-embedded rods, including effects of pre-stress, Composite Structures 184 (2018) 650–661, https://doi.org/10.1016/j.compstruct.2017.10.027.

[17] P. Neto, J. Alfaiate, L. Valarinho, J. Correia, F. Branco, J. Vinagre, Glass beams reinforced with GFRP laminates: Experimental tests and numerical modelling using a discrete strong discontinuity approach, Engineering Structures 99 (2015) 253–263, https://doi.org/10.1016/j.engstruct.2015.04.002.

[18] L. Valarinho, J.R. Correia, F. Branco, Experimental study on the flexural behaviour of multi-span transparent glass-GFRP composite beams, Construction and Building Materials 49 (2013) 1041–1053, https://doi.org/10.1016/j.conbuildmat.2012.11.024.

[19] L. Valarinho, J. Sena-Cruz, J. Correia, F. Branco, Numerical simulation of the flexural behaviour of composite glass-GFRP beams using smeared crack models, Composites Part B: Engineering 110 (2017) 336–350, https://doi.org/10.1016/j.compositesb.2016.10.035.

[20] K. Martens, R. Caspeele, J. Belis, Development of composite glass beams - A review, Engineering Structures 101 (2015) 1–15, https://doi.org/10.1016/j.engstruct.2015.07.006.

[21] S. Jordão, M. Pinho, J. Martin, A. Santiago, L. Neves, Behaviour of laminated glass beams reinforced with pre-stressed cables, Steel Construction 7 (2014) 204–207, https://doi.org/10.1002/stco.201410027.

[22] J. Cupać, C. Louter, A. Nussbaumer, Post-tensioning of glass beams: Analytical determination of the allowable pre-load, Glass Structures and Engineering 6 (2021) 233–248, https://doi.org/10.1007/s40940-021-00150-0.

[23] J.M. Jani, M. Leary, A. Subic, M.A. Gibson, A review of shape memory alloy research, applications and opportunities, Materials and Design 56 (2014) 1078–1113, https://doi.org/10.1016/j.matdes.2013.11.084.

[24] A. Cladera, B. Weber, C. Leinenbach, C. Czaderski, M. Shahverdi, M. Motavalli, Iron-based shape memory alloys for civil engineering structures: An overview, Construction and Building Materials 63 (2014) 281–293, https://doi.org/10.1016/j.conbuildmat.2014.04.032.

[25] B. Asgarian, S. Moradi, Seismic response of steel braced frames with shape memory alloy braces, Journal of Constructional Steel Research 67 (2011) 65–74, https://doi.org/10.1016/j.jcsr.2010.06.006.

[26] L. Dieng, G. Helbert, S.A. Chirani, T. Lecompte, P. Pilvin, Use of shape memory alloys damper device to mitigate vibration amplitudes of bridge cables, Engineering Structures 56 (2013) 1547–1556, https://doi.org/10.1016/j.engstruct.2013.07.018.

[27] A. Hosseini, J. Michels, M. Izadi, E. Ghafoori, A comparative study between Fe-SMA and CFRP reinforcements for prestressed strengthening of metallic structures, Construction and Building Materials 226 (2019) 976–992, https://doi.org/10.1016/j.conbuildmat.2019.07.169.

[28] M. Izadi, A. Hosseini, J. Michels, M. Motavalli, E. Ghafoori, Thermally activated iron-based shape memory alloy for strengthening metallic girders, Thin-Walled Structures 141 (2019) 389–401, https://doi.org/10.1016/j.tws.2019.04.036.

[29] J. Michels, M. Shahverdi, C. Czaderski, Flexural strengthening of structural concrete with iron-based shape memory alloy strips, Structural Concrete 19 (2017) 876–891, https://doi.org/10.1002/suco.201700120.

[30] M. Shahverdi, J. Michels, C. Czaderski, M. Motavalli, Iron-based shape memory alloy strips for strengthening RC members: Material behavior and characterization, Construction and Building Materials 173 (2018) 586–599, https://doi.org/10.1016/j.conbuildmat.2018.04.057.

[31] M. Shin, B. Andrawes, Experimental investigation of actively confined concrete using shape memory alloys, Engineering Structures 32 (2010) 656–664, https://doi.org/10.1016/j.engstruct.2009.11.012.

[32] H. Rojob, R. El-Hacha, Self-prestressing using iron-based shape memory alloy for flexural strengthening of reinforced concrete beams, ACI Materials Journal 114 (2017) 523–532, https://doi.org/10.14359/51689455.

[33] M.R. Izadi, E. Ghafoori, M. Shahverdi, M. Motavalli, S. Maalek, Development of an iron-based shape memory alloy (Fe-SMA) strengthening system for steel plates, Engineering Structures 174 (2018) 433–446, https://doi.org/10.1016/j.engstruct.2018.07.073.

[34] S. Kajiwara, Characteristic features of shape memory effect and related transformation behavior in Fe-based alloys, Materials Science and Engineering A 273–275 (1999) 67–88, https://doi.org/10.1016/s0921-5093(99)00290-7.

[35] A. Sato, E. Chishima, K. Soma, T. Mori, Shape memory effect in $\gamma \rightleftarrows \epsilon$ transformation in Fe-30Mn-1Si alloy single crystals, Acta Metallurgica 30 (1982) 1177–1183, https://doi.org/10.1016/0001-6160(82)90011-6.

[36] A. Sato, H. Kubo, T. Maruyama, Mechanical properties of Fe-Mn-Si based SMA and the application, Materials Transactions 47 (2006) 571–579, https://doi.org/10.2320/matertrans.47.571.

[37] Z. Dong, U.E. Klotz, C. Leinenbach, A. Bergamini, C. Czaderski, M. Motavalli, A novel Fe-Mn-Si shape memory alloy with improved shape recovery properties by VC precipitation, Advanced Engineering Materials 11 (2009) 40–44, https://doi.org/10.1002/adem.200800312.

[38] E. Ghafoori, E. Hosseini, C. Leinenbach, J. Michels, M. Motavalli, Fatigue behavior of a Fe-Mn-Si shape memory alloy used for prestressed strengthening, Materials and Design 133 (2017) 349–362, https://doi.org/10.1016/j.matdes.2017.07.055.

[39] M. Shahverdi, C. Czaderski, M. Motavalli, Iron-based shape memory alloys for prestressed near-surface mounted strengthening of reinforced concrete beams, Construction and Building Materials 112 (2016) 28–38, https://doi.org/10.1016/j.conbuildmat.2016.02.174.

[40] C. Czaderski, M. Shahverdi, R. Brönnimann, C. Leinenbach, M. Motavalli, Feasibility of iron-based shape memory alloy strips for prestressed strengthening of concrete structures, Construction and Building Materials 56 (2014) 94–105, https://doi.org/10.1016/j.conbuildmat.2014.01.069.

[41] J. Michels, M. Shahverdi, C. Czaderski, R. El-Hacha, Mechanical performance of iron-based shape-memory alloy ribbed bars for concrete prestressing, ACI Materials Journal 115 (2018) 877–886, https://doi.org/10.14359/51710959.

[42] M. Shahverdi, C. Czaderski, P. Annen, M. Motavalli, Strengthening of RC beams by iron-based shape memory alloy bars embedded in a shotcrete layer, Engineering Structures 117 (2016) 263–273, https://doi.org/10.1016/j.engstruct.2016.03.023.

[43] C. Leinenbach, W.J. Lee, A. Lis, A. Arabi-Hashemi, C. Cayron, B. Weber, Creep and stress relaxation of a FeMnSi-based shape memory alloy at low temperatures, Materials Science and Engineering A 677 (2016) 106–115, https://doi.org/10.1016/j.msea.2016.09.042.

[44] W.J. Lee, R. Partovi-Nia, T. Suter, C. Leinenbach, Electrochemical characterization and corrosion behavior of an Fe-Mn-Si shape memory alloy in simulated concrete pore solutions, Materials and Corrosion 67 (2016) 839–846, https://doi.org/10.1002/maco.201508701.

[45] W.J. Lee, B. Weber, G. Feltrin, C. Czaderski, M. Motavalli, C. Leinenbach, Stress recovery behaviour of an Fe–Mn–Si–Cr–Ni–VC shape memory alloy used for prestressing, Smart Materials and Structures 22 (2013), 125037, https://doi.org/10.1088/0964-1726/22/12/125037.

[46] Z. Deng, V. Silvestru, J. Michels, L. Li, E. Ghafoori, Performance of Glass to Iron-based Shape Memory Alloy Adhesive Shear Joints with Different Geometry. CGC8, in: 8th International Conference on the Architectural and Structural Application of Glass, Ghent, Belgium, 2022, https://doi.org/10.47982/cgc.8.397.

[47] V. Silvestru, Z. Deng, J. Michels, L. Li, E. Ghafoori, A. Taras, Application of an iron-based shape memory alloy for post-tensioning glass elements, Glass Structures and Engineering 7 (2022) 187–210, https://doi.org/10.1007/s40940-022-00183-z.

[48] V. Silvestru, Z. Deng, J. Michels, A. Taras, Enabling a Ductile Failure of Laminated Glass Beams with Iron-Based Shape Memory Alloy (Fe-SMA) Strips, in: The International Colloquium on Stability and Ductility of Steel Structures, Ernst & Sohn GmbH, Aveiro, Portugal:, 2022,, https://doi.org/10.1002/cepa.

[49] C. Leinenbach, H. Kramer, C. Bernhard, D. Eifler, Thermo-mechanical properties of an Fe-Mn-Si-Cr-Ni-VC shape memory alloy with low transformation temperature, Advanced Engineering Materials 14 (2012) 62–67, https://doi.org/10.1002/adem.201100129.

[50] GOM, Correlate Software and Online Documentation, Rev. 121188 (2019).

[51] J. Rocha, J. Sena-Cruz, E. Pereira, Tensile behaviour of CFRP-glass adhesively bonded connections: double-lap joint tests and numerical modelling, Engineering Structures 260 (2022) 114212, https://doi.org/10.1016/j.engstruct.2022.114212.

[52] S. Nhamoinesu, M. Overend. The mechanical performance of adhesives for a steel-glass composite façade system. Challenging Glass 3: Conference on Architectural and Structural Applications of Glass, CGC 2012, Delft, Netherlands: 2012, p. 293–306. 10.3233/978-1-61499-061-1-293.

[53] E. Hosseini, E. Ghafoori, C. Leinenbach, M. Motavalli, S.R. Holdsworth, Stress recovery and cyclic behaviour of an Fe-Mn-Si shape memory alloy after multiple thermal activation, Smart Materials and Structures (2018) 27, https://doi.org/10.1088/1361-665X/aaa2c9.

[54] F. Veer, T. Riemslag, T. Romein. The failure strength of glass, a non transparent value. Glass Performance Days, Tempere, Finland: 2007, p. pages 610–614.

[55] W. Wang, L. Li, A. Hosseini, E. Ghafoori, Novel fatigue strengthening solution for metallic structures using adhesively bonded Fe-SMA strips: A proof of concept study, International Journal of Fatigue 148 (2021), 106237, https://doi.org/10.1016/j.ijfatigue.2021.106237.

[56] Simulia. ABAQUS computer software and Online Documentation. v6.12. 2012.

[57] M.Feldmann, R. Kasper, B. Abeln. Guidance for European Structural Design of Glass Components. Report EUR 26439 EN. Luxembourg: 2014. doi:10.2788/5523.